A multi-order smoothed particle hydrodynamics method for cardiac electromechanics with the Purkinje network

Chi Zhang[a], Hao Gao[b], Xiangyu Hu[a,*]

[a] *TUM School of Engineering and Design, Technical University of Munich, 85748 Garching, Germany*
[b] *School of Mathematics & Statics, University of Glasgow, Glasgow, UK*

Abstract

In previous work, Zhang et al. (2021) [1] developed an integrated smoothed particle hydrodynamics (SPH) method to simulate the principle aspects of cardiac function, including electrophysiology, passive and active mechanical response of the myocardium. As the inclusion of the Purkinje network in electrocardiology is recognized as fundamental to accurately describing the electrical activation in the right and left ventricles, in this paper, we present a multi-order SPH method to handle the electrical propagation through the Purkinje system and in the myocardium with monodomain/monodomain coupling strategy. We first propose an efficient algorithm for network generation on arbitrarily complex surface by exploiting level-set geometry representation and cell-linked list neighbor search algorithm. Then, a reduced-order SPH method is developed to solve the monodomain equation to characterize the fast electrical activation through the Purkinje network. Finally, a multi-order coupling paradigm is introduced to capture the coupled nature of potential propagation arising from the interaction between the network and the myocardium. A set of numerical examples are studied to assess the computational performance, accuracy and versatility of the proposed method. In particular, numerical study performed in realistic

*Corresponding author.
Email addresses: c.zhang@tum.de (Chi Zhang), hao.gao@glasgow.ac.uk (Hao Gao), xiangyu.hu@tum.de (Xiangyu Hu)

left ventricle demonstrates that the present method features all the physiological issues that characterize a heartbeat simulation, including the initiation of the signal in the Purkinje network and the systolic and diastolic phases. As expected, the results underlie the importance of using physiologically realistic Purkinje network for modeling cardiac function.

Keywords: Cardiac modeling, Purkinje network, Smoothed particle hydrodynamics, Multi-order coupling

---

1. Introduction

Cardiac diseases due to complex mechanisms represent one of the most important category of problems in public health, effecting millions of people each year according to the report of World Health Organization (WHO) [2]. Computational study of cardiac function has received tremendous efforts and is recognized as the community's *next microscope, only better* [3]. Since the heart's physiology involves multiple physics systems, e.g. electrophysiology, (passive and active) mechanics and hemodynamics, an effective integrated computational model is very challenging and requires accurate coupling of all these biophysical systems and asks for advanced numerical techniques [4]. Despite of substantial efforts on integrated cardiac modeling, including fluid-structure interaction (FSI) and fluid-structure-electrophysiology interaction (FSEI), by applying the finite-element method (FEM) [5, 6] and the immersed-boundary method (IBM) [7]. An integrative model capable of simulating the fully coupled cardiac function is still in its infancy due to the meshing bottlenecks of the FEM and the Lagrangian-Eulerian mismatches on the kinematics of the IBM.

As an alternative, the meshless, fully Lagrangian smoothed particle hydrodynamics (SPH) [8, 9] method has shown peculiar advantages in handling multi-physics problems [10, 11] thanks to its very feature of representing each subsystem by an ensemble of particles. Since its original inception by Lucy [8] and Gingold and Monaghan [9] for astrophysical applications, the SPH method has been successfully applied in a broad variety of applications ranging from

fluid mechanics [12, 13, 14, 15] and solid dynamics [16, 17, 18, 19, 20, 21, 22] to multi-phase flows [23, 24, 25] and FSI [26, 27, 28, 29, 30]. More recently, Zhang et al. [1] developed an integrative SPH method for cardiac function and demonstrated its robust and accuracy in dealing with the following aspects : (i) correct capturing of the stiff dynamics of the transmembrane potential and the gating variables, (ii) robust predicting of the large deformations and the strongly anisotropic behavior of the myocardium, (iii) proper coupling of the electrical excitation and the tissue mechanics for electromechanical feedback. This achievement render the SPH method a potential and powerful alternative that can augment the current line of total heart modeling. As the inclusion of the Purkinje network in modeling of the cardiac electrophysiology has been recognized as fundamental to accurately describing the electrical activation in the left and right ventricles [31, 32, 33], developing proper SPH model to handle the electrical propagation through the Purkinje network and in the myocardium is essential for developing an meshless total heart simulator and exploring possible clinical applications.

The electrical activation in the human heart originates in the sinoatrial (SA) node located in the right atrium, travels through the atria and enters the atrioventricular (AV) node [34]. Through the His bundle, the AV node is connected to the Purkinje network which branches from the basal septum into the left and right ventricles. In physiological condition, the action potential travels along the Purkinje network and enters the ventricular muscle through the Purkinje-muscle junctions (PMJ) [31]. The Purkinje network is located in the sub-endocardium and composed of specialized fast-conducting cells to conduct the potential wave efficiently and rapidly [35]. As a key component of the cardiac excitation system, the Purkinje network plays a key role in both physiological excitation and life threatening pathological excitation, i.e., arrhythmia [4]. Therefore, developing algorithms for network generation on complex endocardial surface and capturing the coupled nature of potential propagation arising from the interaction between the Purkinje network and the myocardium is a fundamental task for realistic cardiac modeling.

Concerning the network generation, several algorithms have been developed in the past decades since the first observation century ago [34] of the Purkinje network for both visualization and simulation purposes [36]. More specifically, three approaches have been proposed for the Purkinje network generation, namely, patient-specific segmentation from ex-vivo images [37, 38], manual procedure based on anatomical knowledge [39, 40] and computational algorithms based on the fractal law [41, 42, 43, 44, 45]. Among these approaches, only the first one allows to recover patient-specific information, however, it is limited by the fact that there is no in vivo image technique available to fully reconstruct the Purkinje network's structure [45]. Having the inherent complexity of the Purkinje network in mind, the manual procedure is excessively complicated and time consuming [43]. Notwithstanding the difficulty to recover patient-specific observation, the fractal law based algorithm, e.g. fractal tree [43], has received more and more attentions due to its easy implementation and versatility of incorporating with available code for computational cardiac electrophysiology [43, 46]. The fractal tree algorithm was first adapted by Abboud et al. [32] to create the Purkinje network to study high-frequency electrocardiograms. In their work [32], the network consists of straight segments and is placed in a simplified ventricle. Then, Ijiri et al. [42] introduced non-straight branches with controllable curvature to generate hierarchical network. One notable improvement contributed to Palamara et al. [45] is on creating patient-specific Purkinje network [33] by using clinical measurements of the electrical activation in the ventricle to locate the PKJs. However, all these algorithms can only generate network for simplified ventricles with regular and smooth surface. More recently, Costabal et al. [43] extended the fractal tree algorithm to create network on irregular surface by introducing a second-step projection. However, this algorithm is excessively computational expensive due to the time consuming triangle search for projecting each newly created node.

As regards the cardiac modeling with inclusion of the Purkinje network, numerical studies have been mainly focused on the myocardium electrophysiology with different coupling strategies, e.g. the eikonal/eikonal model [33],

the eikonal/monodomain model [44], the bidomain/bidomain model [47], the monodomain/bidomain model [48], and the monodomain/monodomain model [49, 50]. Here, the first model refers to the one used for the Purkinje network and the second to that applied for the myocardium. As reported by Vergara et al. [50], the monodomain/monodomain coupling model, termed as MM model hereafter, is able to capture many characteristic features of the electrical propagation in the ventricles, and allows to highly reduce the computational time with respect to the eikonal and bidomain models. Another notable feature of the MM model is that it is particularly suited in view of the electromechanical coupling which is one of the main object of this work. Therefore, we consider the MM model in this paper. Notwithstanding significant efforts have been devoted to the numerical studies of cardiac electrophysiology with inclusion of the Purkinje network, rare works in the literature have been devoted to study the Purkinje network's effects on the mechanical contraction of the ventricles. Usyk et al. [51] included the fast conduction of the Purkinje network in a numerical model of cardiac electromechanics through a surrogate spatial modification of the myocardial conduction property. More recently, Landjuela et al. [52] conducted a numerical study of the electromechanical coupling in the left ventricle with presence of the Purkinje network by applying the monodomain/bidomain model within the FEM framework. Despite relentless progress in computational cardiac electrophysiology and electromechanics with inclusion of the Purkinje network within the FEM framework, there is no SPH model has been developed, to the best knowledge of the authors, to study the electrical activation through the Purkinje network and in the myocardium despite the fact that the SPH method has been recognized as an emerging and promising alternative for cardiac modeling [1, 53, 54, 55, 56] and other biomechanics applications [55].

In this work, we start from developing an efficient algorithm based on the fractal law for network generation on non-smooth surface by adapting level-set method and exploiting cell-link list (CLL) scheme. With the geometry representation using level-set method, a three-dimensional fractal tree can be projected onto arbitrarily complex surface, allowing the Purkinje network generation on

the endocardial surface of realistic ventricles. Another key feature of exploiting level-set method is that the time-consuming neighboring triangles search for each newly created node for second-step node projection [43] is avoided. Different with Ref. [43] where a k-d tree scheme is applied for nearest node search, the CLL scheme is adapted in the present algorithm to incorporate with the SPH framework. Also note that, as level-set method is also widely used in medical image segmentation [57], the present approach makes it possible to generate Purkinje network on an image segmentation of human heart. Subsequently, we introduce a reduced-order SPH method for solving monodomain equation on linear structure in three-dimensional space. The key idea is to constrain the degree of freedom along one space dimension other than applying the reduced-order discretization. With exploiting the operator splitting combined with reaction-by-reaction splitting and the anisotropic diffusion SPH discretization proposed in Ref. [1], the present reduced-order SPH method can correctly capture the fast electrical activation in the Purkinje network. Furthermore, a multi-order coupling scheme is developed for MM coupling in the network and myocardium interaction. More precisely, the terminal particles of the reduced-order SPH model of the network, which represent the PKJs, take the roles as excitation sources of current flux to the myocardium particles. To optimize the computational efficiency, a multi-time stepping scheme is proposed for time integration of the corresponding electrophysiology and electromechanics coupling problems. In addition, the proposed multi-order SPH method is integrated to predict the active response of myocardium by implementing the active stress approach [1, 58]. A set of numerical examples, e.g. the potential propagation in a myocardium fiber, cuboid myocardium with inclusion of a generic network, electrophysiology and electromechanics in a realist left ventricle with inclusion of the Purkinje network are computed to demonstrate the accuracy, robustness and feasibility of the proposed multi-order SPH method.

This manuscript is organized as follows. Section 2 introduces the basic principles of the kinetics and the governing equations describing the evolution of the transmembrane potential, and the passive and active mechanical responses

of the tissue. Section 3 presents the efficient algorithm for network generation. In Section 4, the proposed reduced-order SPH method for solving monodomain equation is fully described. Then, the multi-order coupling algorithm and multi-time stepping scheme are detailed in Section 5. A set of examples are included in Section 6 and the concluding remarks and a summary of the key contributions of this paper are given in Section 7. For a better comparison and future openings for in-depth studies, all the computational codes and data-sets accompanying this work are released in the repository of SPHinXsys [59, 60] at `https://www.sphinxsys.org`.

2. Governing equations

In this section, we briefly summarize the governing equations for the passive and active mechanical response of the myocardium, and the electrical activations through the Purkinje network and in the myocardium.

2.1. Kinematics

To characterize the deformation of a continuum, a material point's initial position $\mathbf{r}^0$ is defined in the initial reference configuration, and its current position $\mathbf{r}$ in the deformed configuration. Note that the superscript $(\bullet)^0$ denotes the quantities at the reference state hereafter. Then the deformation tensor $\mathbb{F}$ can be defined by the gradient of current position with respect to the initial reference configuration as

$$\mathbb{F} = \frac{\partial \mathbf{r}}{\partial \mathbf{r}^0} = \nabla^0 \mathbf{u} + \mathbb{I}, \tag{1}$$

where ∇^0 denotes the spatial gradient operator with respect to the initial reference configuration, $\mathbf{u} = \mathbf{r} - \mathbf{r}^0$ the displacement of the material point and $\mathbb{I}$ the unit matrix. Having the deformation tensor $\mathbb{F}$, the right Cauchy-Green deformation tensor is given by

$$\mathbb{C} = \mathbb{F}^T \cdot \mathbb{F}. \tag{2}$$

Associated with $\mathbb{C}$, there are the principle invariants, i.e.,

$$I_1 = \operatorname{tr}\mathbb{C}, \quad I_2 = \frac{1}{2}\left[I_1^2 - \operatorname{tr}(\mathbb{C}^2)\right], \quad I_3 = \det(\mathbb{C}) = J^2, \tag{3}$$

where $J = \det(\mathbb{F})$, and 3 other independent invariants due to the directional preferences

$$I_{ff} = \mathbb{C} : \mathbf{f}^0 \otimes \mathbf{f}^0, \quad I_{ss} = \mathbb{C} : \mathbf{s}^0 \otimes \mathbf{s}^0, \quad I_{fs} = \mathbb{C} : \mathbf{f}^0 \otimes \mathbf{s}^0, \tag{4}$$

where $\mathbf{f}^0$ and $\mathbf{s}^0$ are the undeformed myocardial fiber and sheet unit direction, respectively.

2.2. Electromechanics

In the total Lagrangian framework, the momentum conservation equation for mechanical response of the myocardium can be expressed as

$$\frac{\mathrm{d}\mathbf{v}}{\mathrm{d}t} = \frac{1}{\rho^0}\nabla^0 \cdot \mathbb{P}, \tag{5}$$

where $\frac{\mathrm{d}\mathbf{v}}{\mathrm{d}t}$ is the material derivative, ρ^0 the density at the initial state and $\mathbb{P}$ the first Piola-Kirchhoff stress tensor.

To characterize the active mechanical response of the myocardium, we consider the active stress approach proposed by Nash and Panfilov [58] where the first Piola-Kirchhoff stress $\mathbb{P}$ can be decomposed into passive and active parts as

$$\mathbb{P} = \mathbb{P}_p + \mathbb{P}_a. \tag{6}$$

Here, the passive component $\mathbb{P}_p$ describes the stress required to obtain a given deformation of the passive response, and the active component $\mathbb{P}_a$ denotes the tension induced by the electrical activation.

To model the passive mechanical response, we modify the strain energy function of Holzapfel and Odgen[61] by ensuring the stress vanishes in the reference

configuration and encompassing the finite extensibility [1] as

$$\begin{aligned}\mathfrak{W} =& \frac{a}{2b}\exp\left[b(I_1-3)\right] - a\ln J + \frac{\lambda}{2}(\ln J)^2 + \\ & \sum_{i=f,s}\frac{a_i}{2b_i}\{\exp\left[b_i\left(I_{ii}-1\right)^2\right]-1\} + \\ & \frac{a_{fs}}{2b_{fs}}\{\exp\left[b_{fs}I_{fs}^2\right]-1\},\end{aligned} \tag{7}$$

where λ is the Lamé parameter. Also, a, b, a_f, b_f, a_s, b_s, a_{fs} and b_{fs} are proper positive material constants with the a parameters having dimension of stress and the b parameters being dimensionless. Similar with Ref. [1], a weakly compressible material model is applied herein by choosing a relative large λ, implying that p is the penalty parameter which represents the compressibility of the material. Then, it is easy to derive the second Piola-Kirchhoff stress $\mathbb{S}$ as

$$\mathbb{S} = 2\sum_j \frac{\partial \mathfrak{W}}{\partial I_j}\frac{\partial I_j}{\partial \mathbb{C}} - p\mathbb{C}^{-1}; \quad j=\{1, ff, ss, fs\}; \quad p = \frac{\partial \mathfrak{W}}{\partial J}. \tag{8}$$

Subsequently, the passive first Piola-Kirchhoff stress $\mathbb{P}_p$ is defined as

$$\mathbb{P}_p = \mathbb{F}\mathbb{S}. \tag{9}$$

Following the active stress approach [58], the active first Piola-Kirchhoff stress $\mathbb{P}_a$ is defined as

$$\mathbb{P}_a = T_a\mathbb{F}\mathbf{f}^0 \otimes \mathbf{f}^0, \tag{10}$$

where T_a represents the active cardiomyocyte contraction stress and its evolution is governed by an ordinary differential equation (ODE) defined as

$$\frac{\mathrm{d}T_a}{\mathrm{d}t} = \epsilon\left(U_m\right)\left[k_a\left(U_m - V_r\right) - T_a\right]. \tag{11}$$

Here, the parameters k_a and V_r control the maximum active force and the resting transmembrane potential. Note that the activation function is given by [62]

$$\epsilon\left(U_m\right) = \epsilon_0 + \left(\epsilon_\infty - \epsilon_{-\infty}\right)\exp\{-\exp\left[-\xi\left(U_m - \overline{V}_m\right)\right]\}, \tag{12}$$

where the limiting values $\epsilon_{-\infty}$ at $U_m \to -\infty$ and ϵ_∞ at $U_m \to \infty$, the phase shift $\overline{V}_m$ and the transition slope ξ will ensure a smooth activation of the muscle traction.

2.3. Monodomain equation

Following the work of Vergara et al. [50], we consider MM model to characterize the electrical activation through the Purkinje network and in the myocardium. In monodomain equation, the evolution of the transmembrane potential U_m is governed by a coupled system of partial differential equations (PDEs) written as

$$C_m \frac{\mathrm{d}U_m}{\mathrm{d}t} = \nabla^0 \cdot \left(\mathbb{D}\nabla^0 U_m\right) + I_{ion}, \tag{13}$$

where C_m denotes the capacitance of the cell membrane, $\mathbb{D}$ the conductivity coefficient and I_{ion} the ionic current. For the electrical activation through the Purkinje network, the conductivity coefficient is $\mathbb{D} = d^P_{iso}\mathbb{I}$ implying a isotropic conductivity. For the electrical activation in the myocardium, the conductivity coefficient is defined with respect to the initial reference configuration by $\mathbb{D} = d^M_{iso}\mathbb{I} + d^M_{ani}\mathbf{f}^0 \otimes \mathbf{f}^0$ with d^M_{iso} denoting the isotropic contribution and d^M_{ani} the anisotropic contribution to account for conductivity along fiber direction $\mathbf{f}^0$.

To close the system of Eq. (13), we apply the Aliev-Panfilow model [63] which has been successfully implemented in the computational cardiac electrophysiology in realistic heart geometry [64] and reads

$$\begin{cases} I_{ion}(U_m, w) = -kU_m(U_m - a)(U_m - 1) - wU_m \\ \frac{\mathrm{d}w}{\mathrm{d}t} = g(U_m, w) = \epsilon(U_m, w)(-kU_m(U_m - b - 1) - w) \end{cases}, \tag{14}$$

where $\epsilon(U_m, w) = \epsilon_0 + \mu_1 w/(\mu_2 + U_m)$ and k, a, b, ϵ_0, μ_1 and μ_2 are proper constant parameters to be specified later.

3. Efficient algorithm for network generation

In this section, an efficient algorithm based on the fractal law for network generation on arbitrarily complex surface is presented. We first summarize the level-set concept and its construction by parsing a computer-aided-design (CAD) model to handle the arbitrarily complex surface representation. Then, the detailed algorithm for network generation is described. Finally, the CLL scheme for nearest node search is presented.

3.1. Surface representation

To represent the arbitrarily complex surface, we consider the level-set method where the geometry surface can be implicit defined by the zero level-set of the signed-distance function

$$\Gamma = \{(x, y, z) \,|\phi\,(x, y, z, t) = 0\}\,, \tag{15}$$

where ϕ is the level-set value. Then, the normal direction $\mathbf{N} = (n_x, n_y, n_z)^T$ of the surface can be computed from

$$\mathbf{N} = \frac{\nabla\phi}{|\nabla\phi|}. \tag{16}$$

To discretize the level-set function, a Cartesian background mesh is generated in the whole computational domain and the level-set value ϕ is equal to the distance from the cell center to the surface. It is worth noting that a negative phase with $\phi < 0$ is defined if the cell center is inside the geometry, while positive phase with $\phi > 0$ otherwise.

To construct the level-set field, we choose to parse the polygon mesh, which can be in STL or OBJ format, of anatomical heart model following our previous work [65, 29]. By parsing the corresponding polygon mesh, the distance from a cell center to the surface can be computed by iterating all triangles to find the nearest triangle and then find the closest point located on the triangle. Also, locating whether a cell is inside the geometry can be conducted by checking the sign of the dot product between the nearest triangle's norm and the vector pointing from the closest point located on the triangle to the given point. The detailed algorithm is summarized as Algorithm 1. Also note that one can build its own triangulation parser or apply a proper open-source library, for example Simbody library [66].

3.2. Algorithm for network generation

Based on the fractal law [42, 43], a three-dimensional network on a non-smooth surface can be generated by iteratively generating branch, which is

Algorithm 1: Level-set initialization by paring polygon mesh.

```
Build a Cartesian background mesh with proper resolution ;
Read and parse the polygon mesh ;
for each cell i do
    Get the cell center r_i ;
    Find the nearest triangle and its norm n_t ;
    Find the closest point r_t on the nearest triangle ;
    Set φ_i = sign((r_i · n_t)) |r_i − r_t| ;
    Comput the normal direction with Eq. (16) ;
end
```

represented as polylines of segments and nodes, with proper constraint and immediately projecting every newly created nodes onto the corresponding surface, e.g. endocardial surface of ventricles.

With assumption of each branch consists of $N-1$ segments and N nodes, the first branch is created by iteratively generating $N-1$ segments with a given initial node denoted as $node_0$, a prescribed growth direction $\mathbf{d}_0$ and a proper segment length l_{seg}. From the terminal of the initial branch, i.e., $node_N$, two *child* branches in different growing direction will be created and this process will be iteratively continued on condition that the branch is marked as *branch-to-grow*. Figure 1 illustrates the iterative process for generating a simple network. Before moving to the detailed algorithm for branch growth, a criterion is introduced for determining whether a branch is continue to grow, namely marked as *branch-to-grow*, or terminate. More precisely, a potential collision detection will be conducted for each newly created node, and the node will be removed and the branch is terminated if a collision detected. Otherwise, a branch is marked as *branch-to-grow* if no collision is detected after all N nodes have been fully generated. The collision criterion is defined as

$$|\mathbf{r}_{new} - \mathbf{r}_{nearest}| \leq \sigma, \tag{17}$$

where $\sigma = 5l_{seg}$ is the threshold, $\mathbf{r}_{new}$ the position of the newly created node and $\mathbf{r}_{nearest}$ the position of the nearest node of all the existing nodes in the network except the ones belonging to the *mother* and *brother* branches. The algorithm for the nearest node search will be presented in the following Section 3.3 by using CLL scheme to incorporate within the SPH framework.

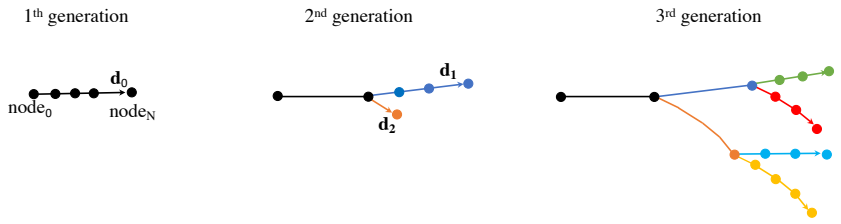

Figure 1: Schematic diagram for iteratively generation branches.

For all the *branch-to-grow* branches, two *child* branches will be generated at their terminal node, namely $node_N$, as shown in Figure 2, with the growing direction defined as

$$\mathbf{d}_i = \frac{\hat{\mathbf{d}_0} + w\mathbf{d}_i^{grad}}{\left|\hat{\mathbf{d}_0} + w\mathbf{d}_i^{grad}\right|}; \quad i = \{1, 2\}, \tag{18}$$

with

$$\hat{\mathbf{d}_0} = \mathbf{d}_0 \cos\alpha + (\mathbf{d}_0 \times \mathbf{N}_0) \sin\alpha. \tag{19}$$

Here, $\mathbf{d}_0$ and $\mathbf{N}_0$ denote the growing direction and normal of $node_N$ belonging to the *mother* branch, i presents the *child* branch index and α the growing angle. Also, w the weight factor and $\mathbf{d}^{grad}$ the gradient of the distance are introduced as repulsion factors to regulate the branch curvature [43]. It can be noted that the initial growing direction of a new *child* branch is determined by the growing direction of $node_N$ belonging to its *mother* branch and the repulsion factors. The same principle governs the segment growth, where the growing direction is determined by the previous one and the repulsion factors as shown in Figure 2. Following Ref. [43], the gradient of the distance is computed with a central finite difference approximation

$$\mathbf{d}^{grad} = \frac{1}{2\epsilon}\left\{\text{dist}\left(\mathbf{r}_0 + \epsilon\mathbf{e}\right) - \text{dist}\left(\mathbf{r}_0 - \epsilon\mathbf{e}\right)\right\}, \tag{20}$$

where $\epsilon = l_{seg}$ is the parameter, $\mathbf{e}$ the Cartesian basis vector, $\mathbf{r}_0$ the position of the previous node and dist $(\bullet)$ function returns the distance of any given point to the closest node found in the network.

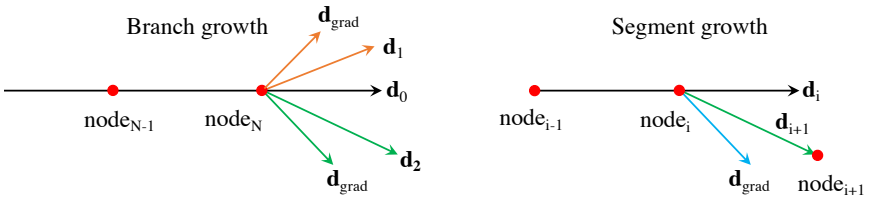

Figure 2: Schematic diagram for one *branch-to-grow* branch growing into two *child* branches and segment growth inside a branch. Each *branch-to-grow* branch will grow into two *child* branches whose directions are given in Eq. (18). For the segment growth, the growth direction is determined by the previous one and the gradient defined in Eq. (20). (For interpretation of the references to color in this figure legend, the reader is referred to the web version of this article.)

To efficiently generate a three-dimensional network on arbitrary complex surface, we immediately project every newly created node onto the surface represented by the level-set method with

$$\begin{cases} \mathbf{r}_{project} = \mathbf{r}_{node} - \phi_{node}\mathbf{N}_{node} \\ \phi_{node} = \phi(\mathbf{r}_{node}) \\ \mathbf{N}_{node} = \mathbf{N}(\mathbf{r}_{node}) \end{cases}, \tag{21}$$

where ϕ_{node} and $\mathbf{N}_{node}$ can be interpolated from the level-set filed. Note that Refs. [42, 43] projected the node onto the surface by using the normal or vortex normal of the neighboring triangular elements. In this case, an immediate difficult relates the computational cost of searching the neighboring triangular elements. This time consuming process is removed in the present algorithm by exploiting the level-set method where projection is straightforward by using trilinear data interpolation.

Similarly to Ref. [43], three kinematic factor, i.e., the segment number $N-1$ and length l_{seg}, the branch angle α and the repulsion factors w and $\mathbf{d}^{grad}$, determine the shape of the network. To embed the network generation with the SPH

framework, the segment number and length will be set as constant parameters without special specification. To introduce randomness to the network generation, we calculate the branch angle by adding a small random number. Also, we shuffle the order of growing branches in each generation to randomly distribute the influence of curvature with respect to existing nodes. The detailed algorithm for generating network is described in Algorithm 2.

3.3. Nearest node search with CLL scheme

Different with the work of Costabal et al. [43] where a k-d tree binary structure is applied for nearest node search, we apply the CLL scheme which is widely used in the particle-based method for neighboring particles search. The CLL works by subdividing the whole computational domain into cells with an cell length greater than or equal to a specific cut-off radius as shown in Figure 3. The nodes are sorted into these cells and the neighbor search are conducted between nodes in the same or neighboring cells. The network generation process can be efficiently embedded into the CLL scheme by added newly created node into its corresponding cell without changing the whole data structure. Note that we set the cutoff radius equals to $2.6l_{seg}$ similar to the one used for the $5th$-order Wendland smoothing kernel [67] which is applied for all the simulations presented in this work.

4. Reduced-order SPH method

In this section, we present a reduced-order SPH method for discretizing the monodomain equation in a linear structure in three-dimensional space, and then the corresponding neighboring particles search is fully described as follows.

4.1. Reduced-order SPH method

To model the electrical activation through the Purkinje network, we derive a reduced-order SPH method to discretize the monodomain equation. Considering that the electrical activation through the Purkinje network is characterized by isotropic wave propagation through three-dimensional space, we can drive a

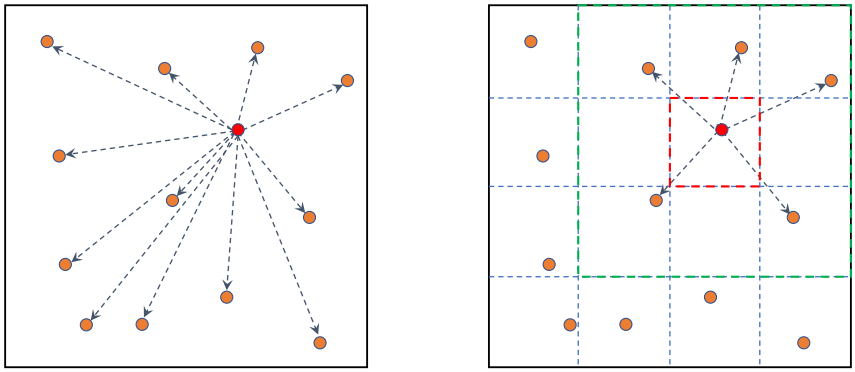

Figure 3: Schematic diagram for the CLL scheme for nearest node search. The neighbor search of a single node can be conducted by searching all other nodes (left panel) or by dividing the domain into cells with an length of at least the cutoff radius and searching the neighbors between the node and all nodes in the same (red) and adjacent (green) cells. Here, we consider the cutoff radius equals to $2.6l_{seg}$ for consistency with the SPH framework. (For interpretation of the references to color in this figure legend, the reader is referred to the web version of this article.)

reduced-order SPH method by constraining the degree of freedom along one space dimension.

In the full-order SPH method [16, 8, 13], the kernel approximation of a continuous function $f(\mathbf{r})$ reads

$$f(\mathbf{r}) \approx \int_{\Omega} f(\mathbf{r}') W(\mathbf{r}-\mathbf{r}', h)\, d\mathbf{r}', \tag{22}$$

where Ω denotes the volume of the integral domain and $W(\mathbf{r}-\mathbf{r}', h)$ the smoothing kernel function with smoothing length h defining the support domain. By carrying out the integration of Eq. (22) along the to-be-reduced dimension, we can rewrite the approximation of $f(\mathbf{r})$ as

$$f(\mathbf{r}) \approx \int_{\widehat{\Omega}} f(\mathbf{r}') \widehat{W}(\mathbf{r}-\mathbf{r}', h)\, d\mathbf{r}', \tag{23}$$

where $\widehat{\Omega}$ denotes the to-be-reduced dimension space and $\widehat{W}$ the reduced-order kernel function. For solving reduced-order problem in three-dimensional space, the integration space is reduced from three to one dimension. Therefore, a

reduced-order fifth-order Wendland kernel [67] reads

$$\widehat{W}(q,h)=\alpha\begin{cases}(1+2q)\left(1-0.5q\right)^{4} & \text{if} \quad 0\leq q\leq 2\\ 0 & \text{otherwise}\end{cases}, \tag{24}$$

where $q=\left|\mathbf{r}-\mathbf{r}'\right|/h$ and the constant α is equal to $\frac{3}{4h}$. Note that the reduced-order kernel function has identical form with the full-order counterpart except different dimensional normalizing constant parameter, allowing the integration of unit can be satisfied in the reduced space.

With Eq. (23) in hand, the gradient of function f reads [1, 16]

$$\nabla f(\mathbf{r})\approx\int_{\widehat{\Omega}}\nabla f(\mathbf{r}')\widehat{W}(\mathbf{r}-\mathbf{r}',h)dV(\mathbf{r}'). \tag{25}$$

Integrating by parts of Eq. (25) with the Gauss theorem yields

$$\nabla f(\mathbf{r})\approx\int_{\partial\widehat{\Omega}}f(\mathbf{r}')\widehat{W}(\mathbf{r}-\mathbf{r}',h)\mathbf{n}dS(\mathbf{r}')-\int_{\widehat{\Omega}}f(\mathbf{r}')\nabla\widehat{W}(\mathbf{r}-\mathbf{r}',h)dV(\mathbf{r}'). \tag{26}$$

Due to the assumption of compact support of the kernel function, the first right-hand-side term of Eq. (26) vanishes. Therefore, the gradient of function f can be approximated by

$$\nabla f\left(\mathbf{r}\right)\approx-\int_{\widehat{\Omega}}f(\mathbf{r}')\nabla\widehat{W}\left(\mathbf{r}-\mathbf{r}',h\right)dV(\mathbf{r}')\approx-\sum_{j}V_{j}f_{j}\nabla_{i}\widehat{W}_{ij}. \tag{27}$$

Here, V is the particle volume, $f_j\equiv f(\mathbf{r}')$ and $\nabla_i\widehat{W}_{ij}\equiv\nabla\widehat{W}(\mathbf{r}-\mathbf{r}',h)$. Subsequently, it's not difficulty to derive the particle approximation of ∇f in symmetric form as

$$\nabla f_i=f_i\nabla 1+\nabla f_i\approx\sum_{j}V_{j}\left(f_i-f_j\right)\nabla_i\widehat{W}_{ij}, \tag{28}$$

and anti-symmetric conservative form

$$\nabla f_i=\nabla f_i-f_i\nabla 1\approx-\sum_{j}V_{j}\left(f_i+f_j\right)\nabla_i\widehat{W}_{ij}. \tag{29}$$

It's worth noting that the symmetric-form approximation of Eq. (28) is used to determine the local structure of a field, while the anti-symmetric conservative form of Eq. (29) is generally applied to compute the surface integration with respect to a variable for solving its conservation law. Due to the anti-symmetric property, i.e. $\nabla_i W_{ij}=-\nabla_j W_{ji}$, it implies conservation of the particle system.

4.2. Kernel Gradient correction

Similar with the full-order SPH scheme, particle approximation of Eq. (27) introduces considerable inconsistency if particle distribution is irregular. To remedy this issue, the kernel gradient correction [17] can be introduced to remediate the boundary deficiency and the inconsistency in particle approximation.

Following Refs. [17, 10, 11], we can Taylor-expand f_j around $\mathbf{r}$

$$f_j = f(\mathbf{r}) + (\mathbf{r}_j - \mathbf{r}) \cdot \nabla f(\mathbf{r}) + O(\mathbf{r}^2), \tag{30}$$

to assess the consistency order of the the particle approximation. Substituting Eq. (30) to Eq. (27) reads

$$\nabla f(\mathbf{r}) \approx -\sum_j V_j \left\{ f(\mathbf{r}) + (\mathbf{r}_j - \mathbf{r}) \cdot \nabla f(\mathbf{r}) \right\} \otimes \nabla \widehat{W}(\mathbf{r} - \mathbf{r}_j, h). \tag{31}$$

It's straightforward to conclude that accurate approximation of $\nabla f(\mathbf{r})$ requires

$$\sum_j V_j \nabla \widehat{W}(\mathbf{r} - \mathbf{r}_j, h) \approx 0, \tag{32}$$

and

$$\sum_j V_j \left(\mathbf{r}_j - \mathbf{r}\right) \nabla \widehat{W}(\mathbf{r} - \mathbf{r}_j, h) \approx \mathbb{I}, \tag{33}$$

where $\mathbb{I}$ is the unit matrix. Eq. (32) is a gradient expression of the partition of unity requirement which can be improved by introducing Shepard filter [17, 11]. To satisfy Eq. (33), the kernel correction matrix $\mathbb{B}$ is introduced and Eq. (33) is rewritten as

$$\sum_j V_j \left(\mathbf{r}_j - \mathbf{r}\right) \mathbb{B}(\mathbf{r}) \nabla \widehat{W}(\mathbf{r} - \mathbf{r}_j, h) = \mathbb{GI}, \tag{34}$$

implying that

$$\mathbb{B}(\mathbf{r}) = \mathbb{G}_i \left(\sum_j V_j \left(\mathbf{r}_j - \mathbf{r}\right) \nabla \widehat{W}(\mathbf{r} - \mathbf{r}_j, h) \right)^{-1}. \tag{35}$$

Here, $\mathbb{G}$ is the rotational matrix given by

$$\mathbb{G}^T = \begin{pmatrix} 1 & 0 & 0 \\ 0 & 0 & 0 \\ 0 & 0 & 0 \end{pmatrix}, \tag{36}$$

which rotates the direction of the linear segment particle i to the unit vector $(0,0,1)$. According to Refs. [17, 68], the introduction of the kernel gradient correction can improve the gradient approximation, while induce extra computational efforts due to the interpolation and matrix inverse. In present framework, this kernel gradient correction only needs to be calculated once at the initial reference configuration, implying that its effect on computational performance can be neglected.

With the kernel gradient correction in hand, the symmetric and anti-symmetric form of Eqs. (28) and (29) can be rewritten as

$$\nabla f_i \approx \sum_j V_j \left(f_i - f_j\right) \overline{\mathbb{B}}_{ij} \nabla_i \widehat{W}_{ij} \tag{37}$$

and

$$\nabla f_i \approx -\sum_j V_j \left(f_i + f_j\right) \overline{\mathbb{B}}_{ij} \nabla_i \widehat{W}_{ij}, \tag{38}$$

respectively. Here, $\overline{\mathbb{B}}_{ij} = (\mathbb{B}_i + \mathbb{B}_j)/2$ represents the average between a interacting particle pair. It's worth noting that the introduction of the kernel gradient correction has negligible effects when the particle distribution is uniform, such as the particles generated by the present network generator.

4.3. Reduced-order SPH discretization for monodomain equation

Following our previous work [1], we employ the operator splitting method to decouple the monodomain equation on the Purkinje network into a PDE

$$S_d \quad : \quad C_m \frac{\mathrm{d}U_m}{\mathrm{d}t} = d_{iso}^P \nabla^2 U_m, \tag{39}$$

and two ODEs

$$S_r \quad : \quad \begin{cases} C_m \frac{\mathrm{d}U_m}{\mathrm{d}t} = I_{ion}(U_m, w) \\ \frac{\mathrm{d}w}{\mathrm{d}t} = g(U_m, w) \end{cases}, \tag{40}$$

where $I_{ion}(U_m, w)$ and $g(U_m, w)$ are defined by the Aliev-Panfilow model [63]. Here, the operators S_d corresponds to the diffusion step and S_r the reaction step, and more details are referred to Ref. [1]. Then, we employ the 2nd-order

Strang splitting [69] to approximate the solution of the monodomain equation from time t to $t + \Delta t$ as

$$U_m\left(t + \Delta t\right) = S_r(\frac{\Delta t}{2}) \circ S_d(\Delta t) \circ S_r(\frac{\Delta t}{2}) U_m\left(t\right), \tag{41}$$

where the $\circ$ symbol separates each operator and indicates that an operator is applied to the following arguments. Similar to Ref. [1], a reaction-by-reaction splitting operator with the quasi-steady-state (QSS) solver is applied for the operator S_r. As for the operator S_d, we apply the standard SPH discretization for dissipative dynamics [70, 13] within the reduced-order framework. Together with Eq. (37), the diffusion step can be discretized by

$$S_d \quad : \quad \frac{\mathrm{d}U_{m,i}}{\mathrm{d}t} = \frac{2d_{iso}^P}{C_m} \sum_j \frac{U_{m,i} - U_{m,j}}{r_{ij}} \mathbf{e}_{ij} \cdot \overline{\mathbb{B}}_{ij} \mathbf{e}_{ij} V_j \frac{\partial \widehat{W}\left(r_{ij}, h\right)}{\partial r_{ij}}, \tag{42}$$

where $U_{m,i}$ and $V_{m,j}$ denote the transmembrane potential of particle i and j, respectively. For isotropic diffusion, Eq. (42) has the similar form with the original form of Monaghan [71] and implies that the contribution to the rate of change of $U_{m,i}$ from particle j is positive if $U_{m,j} > U_{m,i}$ as $\mathbf{e}_{ij} \cdot \overline{\mathbb{B}}_{ij} \mathbf{e}_{ij} V_j \frac{\partial \widehat{W}(r_{ij},h)}{\partial r_{ij}} \leq 0$, indicating the the second law of thermodynamics is guaranteed. Also, as presented by Monaghan [71], the approximation of Eq. (42) is conservative due to its anti-symmetric form. With the kernel gradient correction, the diffusion operator of Eq. (42) approximately achieves first-order consistency. As for the anisotropic diffusion in the myocardium, we employ the anisotropic SPH discretization presented in Ref. [1] to address the issue of non-physical diffusion. Also note that, the approximation of Eq. (42) can be further improved by the scheme of Fatehi and Manzari [72], which is consistent enough to exactly predict the second derivative of a quadratic function, with sacrificing of computational efficiency.

4.4. Network-based neighboring particle search

Having the network generated, the corresponding particle discretization can be initialized by converting each node to one particle and assigning the particle volume $l_g * A_b$ in the reduced-order scheme. As we assume the cross-section

A_b is constant for the the network branches. Therefore, although not explicitly defined, the choice of A_b does not change the diffusive dynamics along the network. To implement the particle interaction configuration, which consists of determining particle-neighbor lists and computing corresponding kernel weights and gradients, we introduce a network-based neighboring particle search scheme.

The working principle of the network-based neighboring particle search scheme is that each particle can only has interactions with particles from its *mother*, *child* and current branches. In this case, the electrical activation resolved by the reduce-order SPH method is characterized by a propagation traveling from a *mother* branch to its *child* branches. Then, the network-based neighboring particles search scheme can be described as follows. As N particles are converted from each branch, they can be categorized into five groups: (1) the particle 0 has two neighboring particles from *mother* branch with indexes N and $N-1$ and another two from current branch with indexes 1 and 2; (2) the particle 1 has one neighboring particles from *mother* branch with index N and another three from current branch with indexes 0, 2 and 3; (3) the particle $N-1$ has one neighboring particle from each *child* branch with index 0 and another three form current branch with index $N-3$, $N-2$ and N; (4) the particle N has two neighboring particles from each *child* branch with indexes 0 and 1, and another two from current branch with indexes $N-2$ and $N-1$; (5) other particle $i \in [2, N-2]$ has four neighboring particles from current branch with indexes $i-2$, $i-1$, $i+1$ and $i+2$. Here, the index denotes the local index of current branch. The present neighboring particle search scheme is illustrated in Figure 4. Following the present process, each particle has $4 \sim 5$ neighboring particles compatible with the smoothing length $h = 1.3dp$ with dp denoting the particle spacing, widely applied for Wendland kernel function. It's worth noting that the smoothing length factor is set as 1.3 to achieve a balance between numerical accuracy and computational efficiency following Ref. [67]. Other values, e.g. 1.5 and 2.0, can have positive effect on the numerical accuracy, while rapidly decrease the computational efficiency.

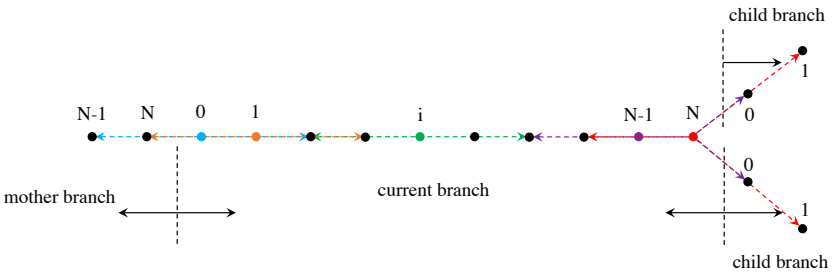

Figure 4: Schematic diagram for the network-based neighboring particle search scheme. The searching domain for typical particles are represented by the arrow line with the same color. Note that the repeated N and $N-1$ denote the particle has similar index, while located in different branch. (For interpretation of the references to color in this figure legend, the reader is referred to the web version of this article.)

5. Multi-order SPH method

In this section, the multi-order SPH method is presented to solve the MM coupling problem between the Purkinje network and the myocardium. Note that, as immersed in the full-order model, the reduced-order particles are assumed not contributing mass and momentum to the full-order model. To optimize the computational efficiency, a multi-time stepping scheme is introduced for the time integration of multi-physics applications.

5.1. Multi-order coupling paradigm

As a subendocardial network, the Purkinje system is characterized by a high conduction velocity and isolated from the muscle, except their PKJs which located on the endocardium. Through these PKJs, the electrical signal enters the myocardium and gives rise a coupling nature of potential propagation. In the present reduced-order SPH method, the PKJs are represented by terminal particles converted from terminal nodes from branches which are terminated due to collision. Then, the terminal particles act as current sources of the full-order myocardium particles located inside their influence region. Similarly to Ref. [50], the influence region is modeled by a spherical region of radius r centered at the PKJ as shown in Figure 5. The influence region can be recovered

straightforwardly by the SPH method due to the fact that each particle has a spherical support domain determined by the cutoff radius.

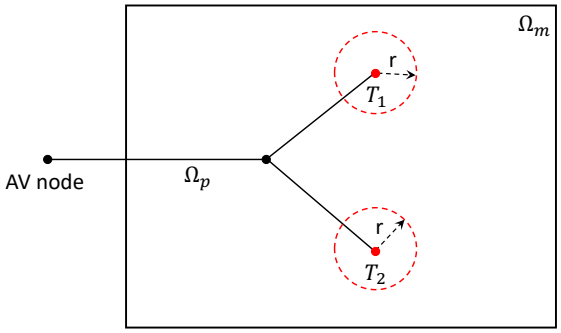

Figure 5: Schematic diagram of a simple myocardial domain Ω_m with a generic network Ω_p. Here, the generic network consists of the AV node and two terminal nodes T_1 and T_2 denoting the PKJs which have the influence of spherical region with a radius of r centered in the node. (For interpretation of the references to color in this figure legend, the reader is referred to the web version of this article.)

For the coupling between reduced-order and full-order structures, namely the Purkinje network and the myocardium, the particles of each coupling pairs are in different level of reduced order. The basic idea is first to transfer the lower-order particles into the high-order particles. Here, we assume that the network terminal particle has the same volume as that in the full-order model. Note again, as we only consider electrical potential coupling, the network particle volume does not contribute mass and momentum to the full dimensional model. Therefore, the coupling is transferred into single-order and the interpolation and interface particle fluxes can be computed. One important property for such coupling in the present project is that the material properties of the coupling structures are not very different. Therefore, coupling between the Purkinje network and the myocardium where terminal particles take the roles of excitation sources can be conducted straightforwardly.

Consider the MM coupling model, the monodomain equation for the myocardium particles located in the influence region of the terminal particles of

the Purkinje network can be rewritten as

$$C_{m,a}\frac{\mathrm{d}U_{m,a}}{\mathrm{d}t} = \nabla\cdot(\mathbb{D}\nabla U_{m,a}) + I_{ion} + I_a^{M:P}, \tag{43}$$

where superscript a represents the myocardium particles and $I_a^{M:P}$ denotes the current flux from network to myocardium. For the myocardium particles located in the influence region of terminal particles, the current flux can be obtained by

$$I_a^{M:P} = 2\left(d_{iso}^M + d_{iso}^P\right)\sum_i V_b' \frac{U_{m,a} - U_{m,b}}{r_{ab}}\frac{\partial W\left(|r_{ab}|, h\right)}{\partial r_{ab}}, \tag{44}$$

where subscript b represents the terminal particles on the network and $V_b' = V_b * A_b = l_{seg}^3$, where A_b presents the cross-section area of the linear segment and is assumed to be uniform, and the kernel function is for three dimensions. Here, we assume that the network and the myocardium particles have identical smoothing length, implying that $l_{seg} = dp_0$ with dp_0 the initial myocardium particle spacing. Then, the neighboring terminal particles from the Purkinje network of a myocardium particle can be searched though the CLL scheme summarized in the previous Section 3.3. Subsequently, the influence region of PKJ represented by the corresponding terminal particle is resolved by a sphere with a radius $r = 2.0h$. It's worth noting that the value of r has a key effect on the coupling nature of potential propagation from PKJs to the myocardium, as observed in Ref. [50]. While a too great value is unable to activate the front in the myocardium, the value of $2.0h$ is able to obtain an instantaneous activation of the myocardium with neglecting the orthodromic delay which will be studied in our future work. Also, this value ensures the numerical consistency as both reduced-order and full-order particles have the same support domain.

5.2. Multi-time stepping scheme

For multi-physics problems, the time integration scheme plays a key role in determining the computational performance. One widely applied approach is the single-time stepping scheme which chooses the minimal time step size of all sub-systems as the applied one and this scheme may induces excessively

computational efforts as demonstrated in Ref. [73]. On the other hand, a multi-time stepping scheme can be introduced to optimize the computational efficiency. For the numerical study of cardiac electromechanics coupling problem of the myocardium with inclusion of the Purkinje network, we have three criteria to determine the time step size for stable time integration. More precisely, the time step size Δt_d^P for solving the monodomain equation in the Purkinje network is given by

$$\Delta t_d^P = \frac{1}{2d}\left(\frac{h^2}{d_{iso}^P}\right), \tag{45}$$

and the Δt_d^M for solving the monodomain equation in the myocardium is determined by

$$\Delta t_d^M = \frac{1}{2d}\left(\frac{h^2}{\mathrm{tr}\,\mathbb{D}}\right). \tag{46}$$

Here, d is the dimensionality and $\mathrm{tr}\,\mathbb{D}$ the trace of the diffusion tensor. As for the mechanical response of the myocardium, the time step size Δt_m^M is defined as

$$\Delta t_m^M = 0.6 \min\left(\frac{h}{c + |\mathbf{v}|_{max}}, \sqrt{\frac{h}{|\frac{\mathrm{d}\mathbf{v}}{\mathrm{d}t}|_{max}}}\right), \tag{47}$$

where c denotes the speed of sound for passive mechanical response. Here, the speed of sound is calculated from $c = \sqrt{\frac{K}{\rho_0}}$ with bulk modulus $K = \frac{2a(1+\nu)}{3(1-2\nu)}$ and ν denoting the Poisson's ratio. Also, $\mathbf{v}|_{max}$ and $|\frac{\mathrm{d}\mathbf{v}}{\mathrm{d}t}|_{max}$ present the maximum velocity and acceleration of the myocardium, respectively. Also note that we assume the three sub-systems has identical smoothing length.

Subsequently, we have three time step sizes, namely Δt_d^P, Δt_d^M and Δt_m^M. In general, the time step size Δt_m^M for mechanical response of the myocardium has the minimal value as it is dominated by the speed of sound. Also, Δt_d^P is smaller than Δt_d^M as the electrical activation travels more rapidly through the Purkinje network than that in the myocardium. With that $\Delta t_d^M > \{\Delta t_d^P, \Delta t_m^M\}$, we introduce the following multi-time stepping method. Other than choosing the minimal step size as the single time step for all the subsystems, we carry out the integration of monodomain equation in the myocardium with Δt_d^M, during which $\varkappa = [\frac{\Delta t_d^M}{\Delta t_d^P}] + 1$ times integration of monodomain equation in the Purkinje network and $\kappa = [\frac{\Delta t_d^M}{\Delta t_m^M}] + 1$ times integration of active mechanical response in the

myocardium are conducted simultaneously. Note that $[\cdot]$ represents the integer operation. The detailed algorithm for the present multi-time stepping algorithm is presented in Algorithm 19. For the time integration of the monodomain and the mechanical response, we apply the coupling scheme of reaction-by-reaction splitting and second-order Runger-Kutta scheme and the position-based Verlet scheme, respectively, and more details are referred to Section 4.4 of Ref. [1].

6. Numerical examples

In this section, we present a set of numerical examples with the aim of assessing the computational efficiency, accuracy and versatility of the proposed methods for numerical study of electromechanics coupling problem of the myocardium with inclusion of the Purkinje network. First of all, we assess the computational efficiency of the proposed algorithm for network generation in comparison with the one presented in Ref. [43]. After this preliminary step, we validate the reduced-order SPH method for resolving the electrical activation through the network. Then, we consider an academic test with simplified myocardium coupled with a generic network to demonstrate the accuracy of the proposed multi-order SPH method with MM coupling model. Having the validations, we apply the present method to approximate the electrophysiology and electromechanics problems of the realistic left ventricle with inclusion of the Purkinje network.

In all the following examples, the full-order $5th$-order Wendland smoothing kernel function with the smoothing lengths $h = 1.3dp$ with dp denoting the initial particle spacing is applied for the resolving the electrical activation and active mechanical response in the myocardium, and more details of the numerical algorithms are referred to our previous work of Ref. [1].

6.1. Computational efficiency of network generation

To assess the computational performance of network generation, we analyze the total CPU time of the present algorithm and the one developed by Costabal et al. [43] where a k-d tree scheme is applied for nearest node search and

the node projection is conducted by directly searching the neighboring triangles. In this work, the computations are carried out on an Intel Xeon CPU E5-2620 v3 2.40GHz desktop computer with 64GB RAM and Scientific Linux system (7.9). Note that the present algorithm is implemented in our open-source SPHinXsys library which is available at `https://www.sphinxsys.org` [59] and the algorithm of Costabal et al. [43] is available in the repository at `https://github.com/fsahli/fractal-trees`.

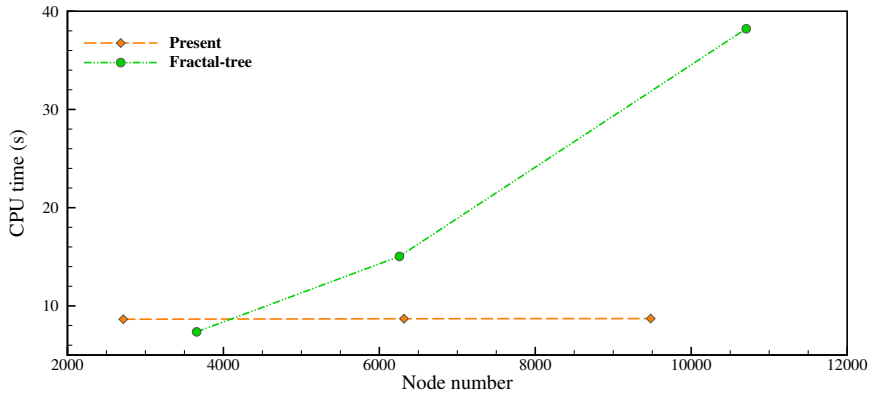

Figure 6: The total CPU time of network generation for different node numbers by using the present algorithm and the one developed by Costabal et al. [43]. (For interpretation of the references to color in this figure legend, the reader is referred to the web version of this article.)

Figure 6 shows the CPU time with respect to network generation with different number of node by using the present algorithm and the one proposed by Costabal et al. [43]. It can be noted that the computational cost of the present algorithm exhibits invisible increase as the increase of the node number. However, the algorithm of Ref. [43] shows linear increase of the computational cost as the increase of the node number due to the fact that neighboring triangle search is essential for every newly created node.

To rigorously analyze the computational performance of the present algorithm, we decompose the total CPU time into two parts, i.e., the pre-processing and the network generation. The pre-processing part includes the parsing of

polygon mesh and the construction of the corresponding level-set field, and the network generation part mainly consists of the iteration process for branch growth. Table 1 reports the computational cost for different parts of the present algorithm for network generation with different node number. The pre-processing part accounts for up to 99% of the total computational time and the network generation part takes less than 1%. This analysis explains why the present algorithm can effectively improve the computational efficiency by avoiding the neighboring triangle search for every newly created node.

6.2. Transmembrane potential propagates through a myocardium fiber

To quantitatively address the accuracy of the proposed reduced-order SPH method for resolving the electrical activation in myocardium fiber, a well-established numerical test where the transmembrane potential propagates through a myocardium fiber is studied in this part. The fiber is considered as linear tissue with the length of $L = 20$mm, and the tissue is assumed to have uniform capacity of $C_m = 1.0$ and isotropic conductivity $d = 0.1\text{mm}^2/\text{ms}$. Following Refs. [74, 75], the ionic current is modeled by the Aliev-Panfilow model [63] with the constant parameters given in Table 2. To activate the depolarization, a stimulus is applied at the discrete level by forcing the transmembrane potential U_m associated to the outermost left particles to $U_m = 1.0$ for time interval $t \in [0, 0.5]$ms, allowing the excitation of a traveling action potential wave rightwards. Note that similar test with considering planar wave propagation over a rectangular slab was conducted in Refs. [74] where the numerical result is available for quantitative comparison. To discretize the fiber, total number of 50 particles are applied in the present simulation.

Figure 7 reports the predicted evolution profile of the transmembrane potential, and its comparison with that reported by Patelli et al. [74]. It is observed that in accordance with the previous numerical estimation [74] and experimental observation [76], the quick propagation of the stimulus through the fiber and the slow decrease in the transmembrane potential after a plateau phase are well predicted by the present reduced-order SPH method. The level of agreement

noted in the comparison with that of Patelli et al. [74] suggests that the present method can accurately resolve the electrical activation in myocardium fiber, and it provides result consistent with those from other state-of-the-art solvers [74, 77].

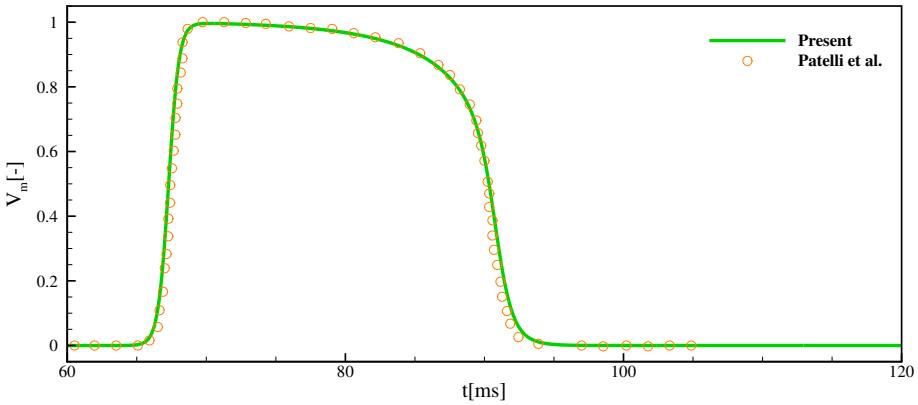

Figure 7: Transmembrane potential propagates through a fiber: The time evolution of the transmembrane potential U_m (green line) superposed with the results reported by Patelli et al. [74] (orange dots). Note that the dimensional counterpart of the transmembrane potential U_m can be recovered by applying the transformation $U_m(\text{mV}) = -80 + 100U_m(-)$. (For interpretation of the references to color in this figure legend, the reader is referred to the web version of this article.)

6.3. Cuboid myocardium with inclusion of a generic network

In this section, we validate the proposed multi-order SPH method. Following Ref. [50], we consider the transmembrane potential propagation in simplified cuboid myocardium with a generic Purkinje network. The myocardium is simplified as a slab with length $l_0 = 40$mm, height $h_0 = 1$mm and width $w_0 = 20$mm, and is modeled by orthogonal material with the fiber and sheet directions parallel to the global coordinates. The Purkinje network consists of three branches with two PKJs interacting with the myocardium as shown in Figure 8. Note that the generic network lied on top of the cuboid domain, similar to physiological situation where the Purkinje fibers are located beneath the endocardium. To activate the transmembrane potential propagation, we apply a stimulus at the

AV node, as shown in Figure 8, allowing the potential travels through the network and enters the myocardium at two PKJs, i.e., $T1$ and $T2$. For validating the coupling paradigm. , the potential profile in the myocardium is probed at point $P1$ located at $(0.75l_0, h_0, 0.5w_0)$. The Aliev-Panfilow model [63] is applied with the constant parameters given in Table 2 for both the myocardium and the network. The diffusion coefficients for myocardium are set as $d^M_{iso} = 0.1\text{mm}^2/\text{ms}$ and $d^M_{ani} = 0.01\text{mm}^2/\text{ms}$, and for network $d^P_{iso} = 0.1\text{mm}^2/\text{ms}$. To discretize the system, the initial particle spacing is set as $dp_0 = h_0/5$ for the myocardium and $l_{seq} = dp_0$ for the network.

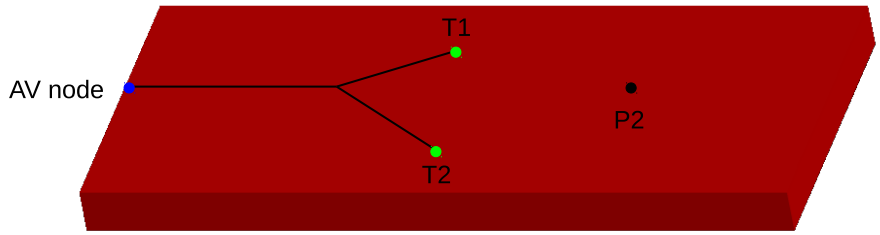

Figure 8: Cuboid myocardium with a generic Purkinje network: The myocardial geometry is simplified as a slab with length $l_0 = 40$mm, height $h_0 = 1$mm and width $w_0 = 20$mm, and the network consists of three branches. The transmembrane potential is initialized at the AV node, travels through the network and then enters the myocardium through two PMJs, i.e., $T1$ and $T2$. The potential probe $P1$ located at the $(0.75l_0, h_0, 0.5w_0)$ where two wave front interacting with each other is applied to probe the potential profile for validating the coupling paradigm.

Figure 9 reports the transmembrane potential traveling through the network and in the myocardium at different time instants. As expected, the potential first travels through the network starting at the AV node, and then enters the myocardium through the PMJs, i.e., $T1$ and $T2$, allowing the activation of the two fronts in the myocardium. It is worth noting that the present multi-order coupling method demonstrates its ability to model in a proper way the collision of two fronts as observed in the frame at $t = 70$ms. **Qualitatively compared with the transmembrane potential reported by Vergara et al. [50] (see Figure 9 in their work), a very similar pattern of the electrical signal**

propagates in the myocardium and forms a proper way of collision of two fronts is noted.

To further investigate the accuracy of the present coupling method, Figure 10 presents the time evolution of the transmembrane potential at point $P1$ located at the myocardium and that through the network. The evolution of the simulated transmembrane potential suggests that the electrical signal activated through the PMJs traveling in the myocardium has the identical profile with that through the network, implying that the energy conservation is guaranteed. Not that an instantaneous activation of the myocardium is applied in the present coupling strategy and the delay in the normal propagation corresponding to the time necessary to excite the myocardial cells [78] will be taken into consideration the the future work.

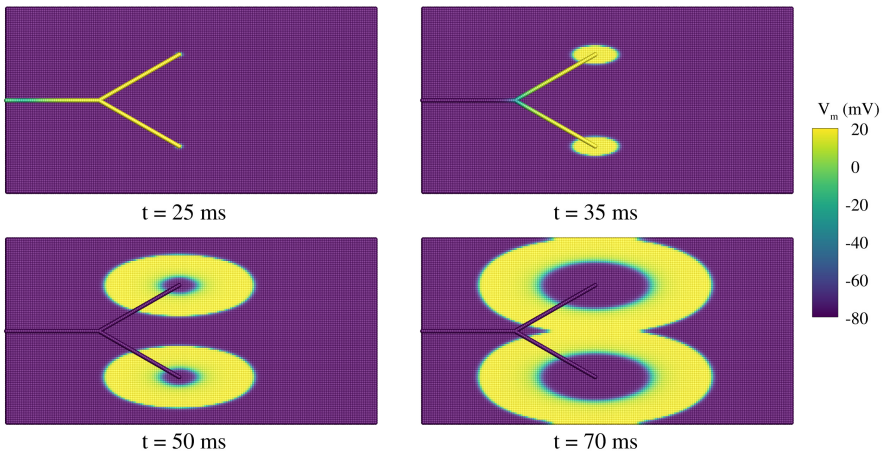

Figure 9: Cuboid myocardium with a generic Purkinje network: Transmembrane potential at different temporal instants. (For interpretation of the references to color in this figure legend, the reader is referred to the web version of this article.)

6.4. Left ventricle with inclusion of the Purkinje network

To demonstrate the versatility of the present multi-order SPH method in realistic cardiac modeling, we consider the transmembrane potential propagation

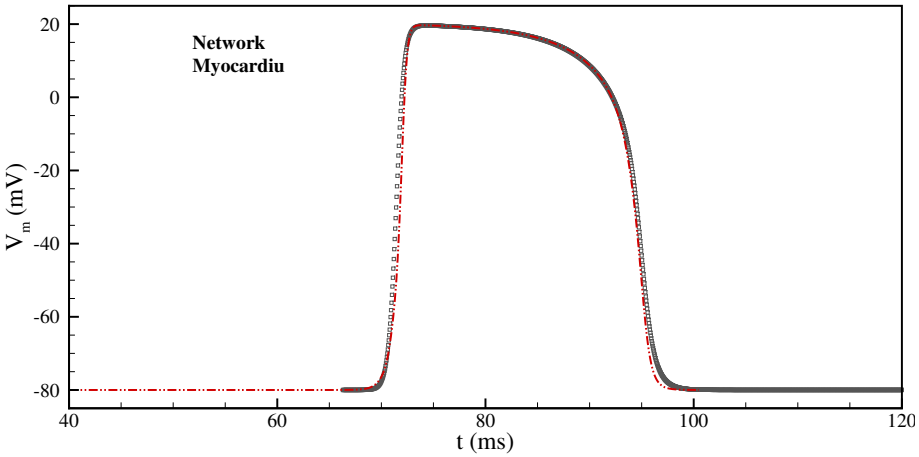

Figure 10: Cuboid myocardium with a generic Purkinje network: The time evolution of the transmembrane potential U_m (red line) observed at $P1$ superposed with the potential profile of that through the network (black dots). (For interpretation of the references to color in this figure legend, the reader is referred to the web version of this article.).

and the corresponding excitation-contraction in the realistic left ventricle with inclusion of the Purkinje network. The left ventricle model applied herein was presented by Gao et al. [5] where a cardiac magnetic resonance (CMR) study was performed on a healthy volunteer. As noted by Ref. [5], this study was approved by the local NHS Research Ethics Committee, and written informed consent was obtained before the CMR scan. Then, the left ventricle geometry and function were imaged with conventional short-axis and long-axis cine images whose parameters are referred to Ref. [5]. From images at early-diastole, the left-ventricle geometry can be constructed using SolidWorks as shown in Figure 11.

Having the left ventricle geometry, we can generate a reduced-order particle model for the Purkinje network on the endocardial surface by using the present network generation algorithm. Figure 11 (bottom panel) illustrates the resulting Purkinje network, which consists of 518 branches and 259 of which are terminal ones. In the reduced-order SPH model, the network is represented by 3888 reduced-order particles and 259 of which are terminal particles which are inter-

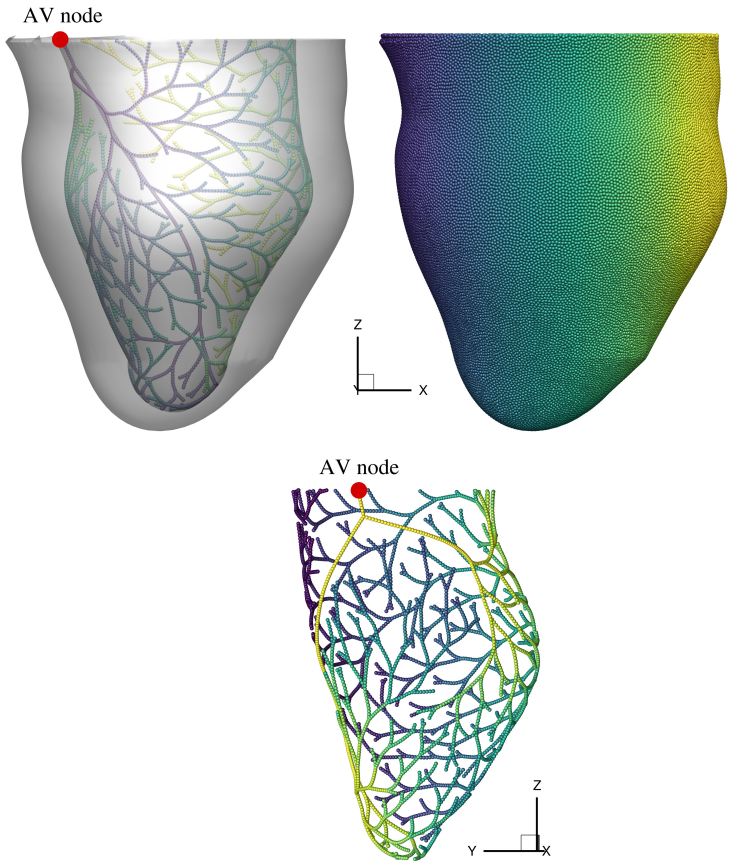

Figure 11: Left ventricle with the Purkinje network: Representations of the left ventricle (upper left panel), the particle model for the left ventricle (upper right panel) and the Purkinje network (bottom panel), respectively. Here, the Purkinje network consists of 3888 reduced-order particles and 259 of which are terminal particles representing PKJs, and the left ventricle is represented by 167209 full-order particles.

acting with the myocardium particles as PKJs. For generating the full-order particle model for the left ventricles, we apply the CAD-BPG mehtod proposed in our previous work [65]. Figure 11 (left panel) shows the particle distribution for the left ventricle and it can be noted that an isotropic particle configuration is obtained and the geometry surface is reasonably well prescribed. Having the particle initialization of the left ventricle, the fiber and sheet reconstructions

are conducted following Ref. [1, 79].

For both electrophysiology and electromechanics study, we consider three cases including, (i) the physiological healthy excitation where the unique source for the Purkinje network is the AV node and the unique sources for the myocardium were the PKJs; (ii) the pathological excitation, namely the Wolff-Parkinson-White syndrome, which is characterized by an extra muscular intramyocardial source in addition to the AV node; (iii) the free-pulse excitation without the Purkinje network where the unique muscular source for the myocardium were located close to the AV node. The Aliev-Panfilow model [63] is applied with the constant parameters given in Table 3. The diffusion coefficient for the myocardium are set as $d^M_{iso} = 0.8\text{mm}^2/\text{ms}$ and $d^M_{ani} = 1.2\text{mm}^2/\text{ms}$, and for the Purkinje network $d^P_{iso} = 22\text{mm}^2/\text{ms}$, indicating that the conduction through the network is 27.5 times faster than that in the myocardium [43].

6.4.1. Electrophysiology

In this part, we present the numerical results of the transmembrane potential propagates in the left ventricle with inclusion of the Purkinje network with different excitation strategies.

Figure 12 reports the transmembrane potential at different time instants through the Purkinje network and in the left ventricle with inclusion of the Purkinje network under physiological and pathological conditions, and without the network. In the Purkinje network, the transmembrane potential activated by a stimulus of $U_m = 1.0$ initiated at the AV node rapidly travels through the network in the free-pulse pattern due to its faster conduction velocity. At the PKJs, which is represented by the terminal particles, the potential enters the myocardium and excites the apex of the left ventricle under physiological healthy condition, allowing non-smooth propagation of wave front. Under pathological condition, which is characterized by an extra muscular source located in the opposite region with respect to the AV node, the left ventricle is excited similarly to the healthy condition with more complex wave front collisions are noted. Note that the pathological test demonstrates the suitability of

the present method in view of the solutions of the MM coupled problem when complex fronts propagate. Without the Purkinje network, the left ventricle is activated via slow smooth diffusion of the transmembrane potential starting at the muscular source, which is located in the region of AV node, and propagating from the base to the apex. Compared with the results obtained without the Purkinje network, the activation sequences with the inclusion of the network exhibits non-smooth potential propagation and rapid excitation from the apex to the base. **Qualitatively compared with the activation sequence reported by Costabal et al. [43] (see Figure 9 in their work), a very similar activation pattern, e.g. non-smooth propagating wavefronts rapidly excite the ventricle from apex to base, is observed in the case with the Purkinje network under physiological condition, while different heart model is noted.**

Figure 13 illustrates the time evolution of the transmembrane potential at the apex with the Purkinje network under physiological and pathological conditions, and without the network. With the purkinje network, the potential propagation under physiological and pathological conditions present identical profile, indicating that the excitation in the apex is dominated by the signals from the network. Compared with the result obtained without the network, the apex is activated much more rapid as expected under both physiological and pathological conditions.

The results reported herein show that the present multi-order SPH method could be applied successfully to model the transmembrane potential propagates in realistic left ventricle with inclusion of the Purkinje network. This represents a crucial step in view of solving a complete electromechanics coupling problem of a realistic ventricle in presence of the Purkinje network.

6.4.2. Electromechanics

In this part, we assess the versatility of the present method for modeling the excitation-contraction of the realistic left ventricle with inclusion of the Purkinje network. Following the previous study for electrophysiology, we consider

the numerical approximation of the active electromechanical response in the left ventricle with different excitation strategies. For the mechanical response, we apply Holzapfel-Ogden model [61] with the constant parameters given in the Table 4 and the active cardiomyocyte contraction stress $T_a = 0.1$ kPa. Note that the Poisson's ratio $\nu = 0.4995$ is applied in the present simulation. For simplicity, the displacement degrees of freedom on the top base of the left ventricle are constrained and the whole heart surface is assumed to be flux-free.

Figure 14 reports excitation-contraction configurations with von Mises stress contour of the left ventricle with the Purkinje network under physiological and pathological conditions, and without the network. For rigorous comparison, the undeformed configuration of the left ventricle is also presented in Figure 14 (left panel). In general, similar contraction pattern, i.e., the excitation-contraction gives rise to the up- and down-ward motions of the apex as the depolarization front traveling in the ventricles, are observed in three conditions. Also, the apex's down-ward motion is accompanied by the physiologically observed wall thickening and the overall torsional motion of the ventricle. Due to the inhomogeneous myocyte orientation distribution incorporated with the anisotropic material model, the physiologically active response through the non-uniform contraction of myofibers are noted. However, compared with the results obtained without the Purkinje network, some remarkable differences can be noted in the deformation pattern due to different electrical activation profiles introduced by the inclusion of the Purkinje network. For example, notable large von Mises stress is exhibited in the regions close to the apex due the fact that the excitation with the inclusion of the Purkinje network is propagates from the apex to the base. It's worth noting that the left ventricle shows larger deformation and more rapid excitation when the Purkinje network is included. As for the physiological and pathological excitations, similarly contraction pattern is noted with small difference in excitation time which will be shown in the following section. Furthermore, Figure 15 presents excitation-contraction configurations with pressure contour. As expected, the general pressure field is

smooth, while exhibits oscillations near the large deformation region. This is reasonable considering that a weakly compressible material model is applied as Ref. [1]. Applying incompressible material model, which is our ongoing work, is of importance to study the mechanical response.

Figure 16 illustrates the time evolution of the z components of the displacements at the apex with three excitation strategies. With inclusion of the Purkinje network, the left ventricle shows larger displacement of the apex with rapid excitation. Compared with the physiological condition, the pathological one induces slightly quick excitation-contraction mechanical response in the ventricle due to the contraction activated by the muscular current source.

The results reported herein show that the present method could be applied successfully to solve the electromechanics coupling problem of the realistic left ventricle with inclusion of the Purkinje network. This represents a crucial step in view of investigating the excitation-contraction profile of an anatomical high-resolution heart model in presence of the Purkinje network, which will be the main objective of our future work.

6.4.3. Computational efficiency

In this paper, we have proposed a multi-time stepping scheme for the time integration of the active electromechanical response of the myocardium with inclusion of the Purkinje network. This part is devoted to rigorously assess the computational performance of the proposed multi-time stepping scheme. We analyze the total CPU time for the simulation of the excitation-contraction of the left ventricle with the presence of the Purkinje network and the computer information is given in Section 6.1. Note that the single-time stepping denotes the time integration where the minimal value of Δt_d^P, Δt_m^M and Δt_m^M is chosen as the time step size.

Table 5 reports the computation time with different time stepping schemes for the electrophysiology and electroemchanics problems of the left ventricle with inclusion of the Purkinje network. It can also be observed that with the present multi-time stepping scheme, one is able to obtain speedup of 36.6 and

28.7 for electrophysiology and electroemchanics simulations, respectively.

7. Concluding remarks

As a pioneering work, this paper presents a multi-order SPH method for cardiac electrophysiology and electromechanics with inclusion of the Purkinje network. The main novelties of the present work are summarized as follows. To the best knowledge of the authors, the following aspects were addressed herein for the first time in developing a meshless approach for total heart modeling,

1. We introduced an efficient algorithm by exploiting level-set geometry presentation and CLL algorithm for network generation on arbitrarily complex surface.
2. We proposed a reduced-order SPH method to resolve the electrical activation in the Purkinje network by solving monodomain equation.
3. We developed a multi-order coupling paradigm to capture the coupled nature of propagation arising from the interaction between the Purkinje network and the myocardium.
4. We presented a multi-time stepping algorithm to optimize the computational efficiency for modeling the electromechanics coupling problem of the myocardium with inclusion of the Purkinje network.

Ultimately, comprehensive and rigorous studies of the potential propagation in myocardium fiber, cuboid myocardium with inclusion of a generic network, electrophysiology and electromechanics coupling problems in the left ventricle with inclusion of the Purkinje network have been conducted. Also, the CPU time is analyzed to assess the computational efficiency of the present network generation and the multi-time stepping algorithms. The results demonstrate the robustness, accuracy and feasibility of the proposed SPH method for cardiac electrophysiology and electromechanics in realistic ventricle with the presence of the Purkinje network.

The multi-order SPH method developed in this work is an essential component of an unified meshless approach to accurately describing the electrical

activation in the left and right ventricles. Based on this work and the previous one [1], the long-term objective of this serial study is developing a multi-physics total-function heart simulator, which has the potential to complement and extend human understanding of cardiac diseases. In particular, one import improvement on the network-myocardium coupling problem would be taking the "pull and push" effect [80, 81, 50], which is due to the fact that the current just before the bifurcation point needs to increase its value in order to be able to stimulate the increased number of cells after the bifurcation, into consideration. Then, complex excitation-contraction example involving real heart geometry will be studied and validated by building cooperation project with researchers in the community. Ultimately, we would like to move to the coupled electromechanics problem of a high-resolution anatomical heart model with four chambers to explore the influence of the patient-specific Purkinje network [45] on local tissue strain distributions and global pressure-volume loops. These insights will help the research community elucidate the interplay between electrical conduction disturbances and the loss of mechanical function.

Algorithm 2: Efficient network generation on arbitrarily complex surface.

```
Parameter setup, e.g. number of iteration N_iteration, number of segments N and length of segment l_seg ;
Given an initial node r_0, initial direction d_0 and branch angle α_0 ;
Do the first generation as shown in Figure 1 ;
Add the first branch to branch-to-grow list ;
for i ≤ N_iteration do
    Shuffle the branch-to-grow list ;
    foreach branch-to-grow do
        for child = 1 to 2 do
            Set branch angle α = α_0 {1.0 + 0.1 * random(−1, 1)} ;
            Compute d̂_0 with Eq. (19) ;
            for j = 1 to N do
                Get the gradient of distance d^grad at r_{j−1} with Eq. (20) ;
                Compute segment direction d_j with Eq. (18) ;
                Create a new node by r_j = r_{j−1} + l_seg * d_j ;
                Project node at r_j to surface with Eq. (21) ;
                Collision detection with Eq. (17) ;
                if collision then
                    Break ;
                end
            end
            if No collision then
                Add the new fully grown bracnh the branch-to-grow list ;
            end
            Set branch angle α = −α ;
        end
    end
end
```

Algorithm 3: The detailed procedure for the time integration using the proposed multi-time stepping scheme for solving electromechanics problem of the myocardium with inclusion of the Purkinje network.

Setup the total simulation time T ;
while $t < T$ **do**
    Compute Δt_d^M with Eq. (46) ;
    Integrate the monodomain qutaion in myocardium with time step size Δt_d^M ;
    Set $t_{sum}^P = 0$;
    while $t_{sum}^P < \Delta t_d^M$ **do**
        Comput Δt_d^P with Eq. (45) ;
        Integrate the monodomain qutaion in the Purkinje network with time step size Δt_d^P ;
        Update sub-integration time with $t_{sum}^P = t_{sum}^P + \Delta t_d^P$;
    end
    Set $t_{sum}^M = 0$;
    while $t_{sum}^M < \Delta t_d^M$ **do**
        Compute Δt_m^M with Eq. (47) ;
        Integrate the mechanical equation in myocardium with time step size Δt_m^P ;
        Update sub-integration time with $t_{sum}^M = t_{sum}^M + \Delta t_m^M$;
    end
    Update the total integration time with $t = t + \Delta t_d^M$;
end
Finalize the Computation ;

Table 1: The analysis of computational cost for different parts of the present algorithm for network generation. The total computational time is decomposed into pre-processing, which consists of the paring of a polygon mesh and the construction of the level-set field, and the network generation part corresponds to iteration process of branch growth.

Number of nodes	Total CPU time(s)	Pre-processing CPU time(s)	Network generation CPU time(s)
2716	8.6423	8.6277	0.0146
6316	8.6929	8.6588	0.0341
9480	8.7113	8.6593	0.052

Table 2: Transmembrane potential propagates through a fiber: Parameters for the Aliev-Panfilow model [63].

k	a	b	ϵ_0	μ_1	μ_2
8.0	0.15	0.15	0.002	0.2	0.3

Table 3: Left ventricle with the Purkinje network: Parameters for the Aliev-Panfilow model [63].

k	a	b	ϵ_0	μ_1	μ_2
8.0	0.01	0.15	0.002	0.2	0.3

Table 4: Left ventricle with the Purkinje network: Parameters for the Holzapfel-Ogden constitution model [61].

$a = 0.059$ kPa	$a_f = 18.472$ kPa	$a_s = 2.841$ kPa	$a_{fs} = 0.216$ kPa
$b = 8.023$	$b_f = 16.026$	$b_s = 11.12$	$b_{fs} = 11.436$

Table 5: Left ventricle with the Purkinje network: Computational efficiency. Here, we evaluate the CPU wall-clock time for computation until the physical time of 10ms.

Cases	Multi-time stepping	Single-time stepping	Speedup
Electrophysiology	5.59s	204.61s	36.6
Electromechanics	11.79s	338.52s	28.7

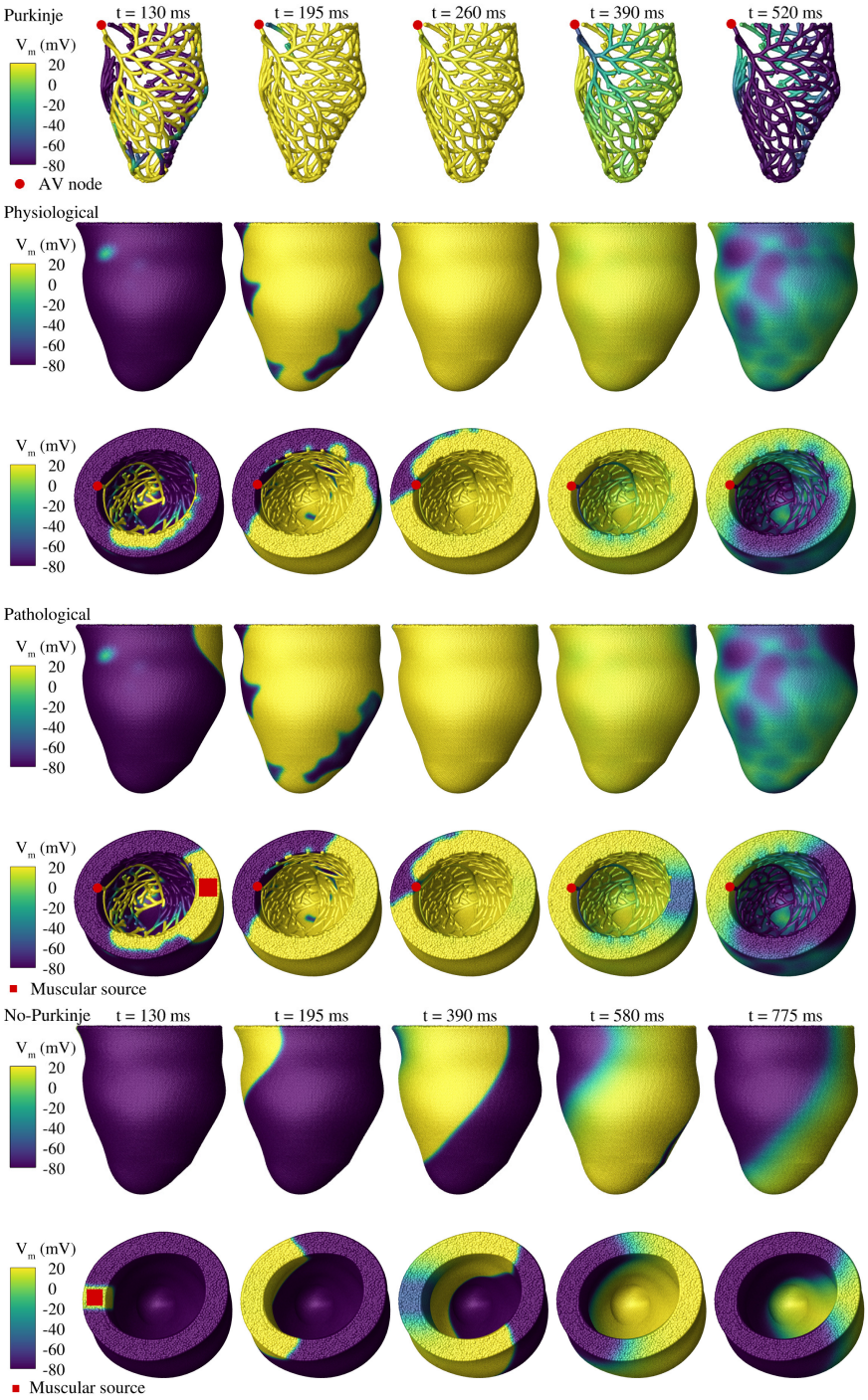

Figure 12: Left ventricle with the Purkinje network: Activation consequences of the ventricle with the Purkinje network under physiological healthy and pathological conditions, and without the network. (For interpretation of the references to color in this figure legend, the reader is referred to the web version of this article.)

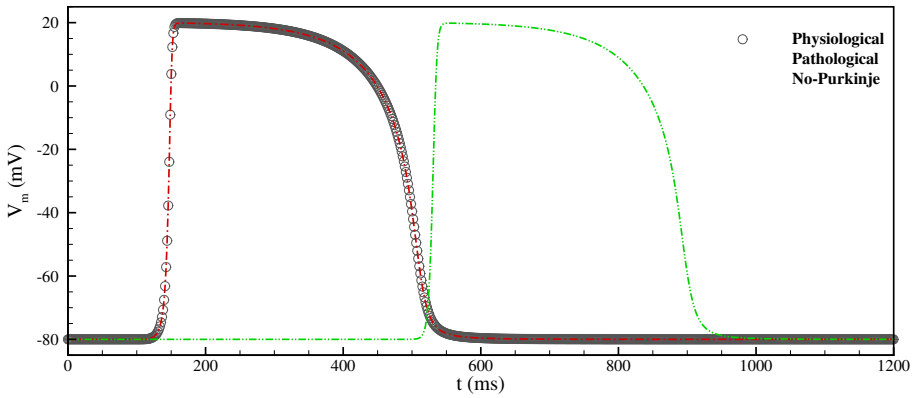

Figure 13: Left ventricle with the Purkinje network: The evolution of transmembrane potential U_m recorded at the apex of the ventricle with the Purkinje network under physiological and pathological conditions, and without the network. (For interpretation of the references to color in this figure legend, the reader is referred to the web version of this article.)

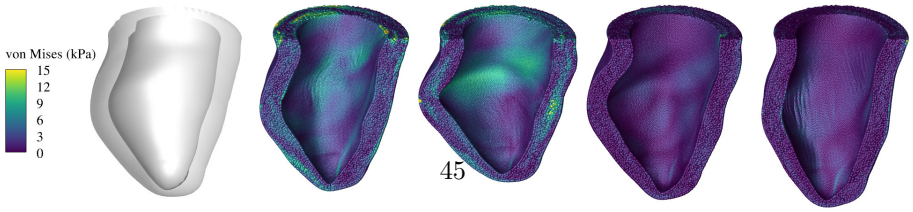

Pathological

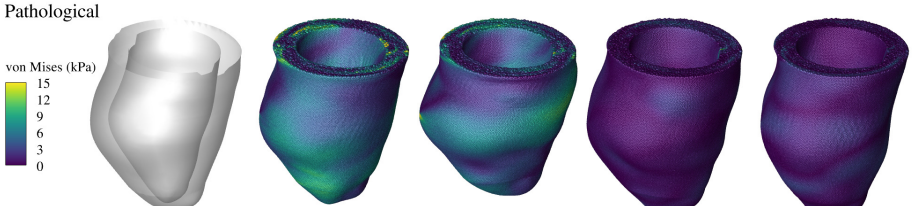

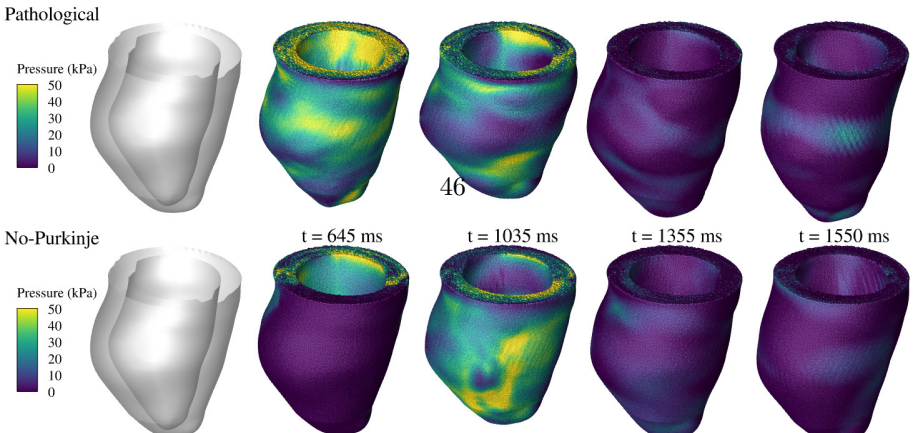
Pathological
Pressure (kPa)
50
40
30
20
10
0
t = 645 ms
t = 1035 ms
t = 1355 ms
t = 1550 ms
No-Purkinje
Pressure (kPa)
50
40
30
20
10
0

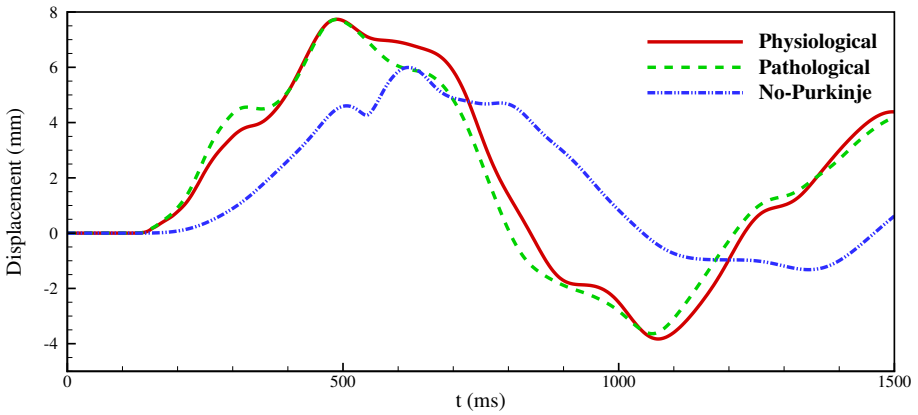

Figure 16: Left ventricle with the Purkinje network: The time history of displacement in the z-axis of the apex of the ventricle with the Purkinje network under physiological and pathological conditions, and without the network. (For interpretation of the references to color in this figure legend, the reader is referred to the web version of this article.)

CRediT authorship contribution statement

Chi Zhang: Conceptualization, Methodology, Investigation, Visualization, Validation, Formal analysis, Writing - original draft, Writing - review & editing; **Hao Gao:** Investigation, Writing - review & editing; **Xiangyu Hu:** Supervision, Methodology, Investigation, Writing - review & editing.

Declaration of competing interest

The authors declare that they have no known competing financial interests or personal relationships that could have appeared to influence the work reported in this paper.

Acknowledgement

C. Zhang and X.Y. Hu would like to express their gratitude to Deutsche Forschungsgemeinschaft (DFG) for their sponsorship of this research under grant numbers DFG HU1527/10-1 and HU1527/12-4.

References

References

[1] C. Zhang, J. Wang, M. Rezavand, D. Wu, X. Hu, An integrative smoothed particle hydrodynamics method for modeling cardiac function, Computer Methods in Applied Mechanics and Engineering 381 (2021) 113847.

[2] W. H. Organization, The top 10 causes of death, `https://www.who.int/news-room/fact-sheets/detail/the-top-10-causes-of-death/`, [Online; accessed 7-July-2021] (2018).

[3] N. A. Trayanova, Whole-heart modeling: Applications to cardiac electrophysiology and electromechanics, Circulation Research 108 (2011) 113–128.

[4] A. Quarteroni, A. Manzoni, C. Vergara, The cardiovascular system: Mathematical modelling, numerical algorithms and clinical applications, Acta Numerica 26 (2017) 365–590.

[5] H. Gao, L. Feng, N. Qi, C. Berry, B. E. Griffith, X. Luo, A coupled mitral valve—left ventricle model with fluid-structure interaction, Medical Engineering & Physics 47 (2017) 128–136.

[6] A. Santiago, J. Aguado-Sierra, M. Zavala-Aké, R. Doste-Beltran, S. Gómez, R. Arís, J. C. Cajas, E. Casoni, M. Vázquez, Fully coupled fluid-electromechanical model of the human heart for supercomputers, International Journal for Numerical Methods in Biomedical Engineering 34 (2018) e3140.

[7] F. Viola, V. Meschini, R. Verzicco, Fluid–structure-electrophysiology interaction (FSEI) in the left-heart: a multi-way coupled computational model, European Journal of Mechanics-B/Fluids 79 (2020) 212–232.

[8] L. B. Lucy, A numerical approach to the testing of the fission hypothesis, The Astronomical Journal 82 (1977) 1013–1024.

[9] R. A. Gingold, J. J. Monaghan, Smoothed particle hydrodynamics: Theory and application to non-spherical stars, Monthly Notices of the Royal Astronomical Society 181 (1977) 375–389.

[10] M. Liu, Z. Zhang, Smoothed particle hydrodynamics (SPH) for modeling fluid-structure interactions, Science ChinaPhysics, Mechanics & Astronomy 62 (2019) 984701.

[11] C. Zhang, Y. Zhu, D. Wu, N. A. Adams, X. Hu, Smoothed particle hydrodynamics: Methodology development and recent achievement, Journal of Hydrodynamics 34.

[12] J. J. Monaghan, Simulating free surface flows with SPH, Journal of Computational Physics 110 (1994) 399–406.

[13] X. Y. Hu, N. A. Adams, A multi-phase SPH method for macroscopic and mesoscopic flows, Journal of Computational Physics 213 (2006) 844–861.

[14] C. Zhang, X. Hu, N. A. Adams, A weakly compressible SPH method based on a low-dissipation riemann solver, Journal of Computational Physics 335 (2017) 605–620.

[15] C. Zhang, G. Xiang, B. Wang, X. Hu, N. A. Adams, A weakly compressible SPH method with WENO reconstruction, Journal of Computational Physics 392 (2019) 1–18.

[16] J. J. Monaghan, Smoothed particle hydrodynamics, Annual Review of Astronomy and Astrophysics 30 (1992) 543–574.

[17] P. Randles, L. D. Libersky, Smoothed particle hydrodynamics: Some recent improvements and applications, Computer Methods in Applied Mechanics and Engineering 139 (1996) 375–408.

[18] J. Bonet, S. Kulasegaram, Correction and stabilization of smooth particle hydrodynamics methods with applications in metal forming simulations, International Journal for Numerical Methods in Engineering 47 (6) (2000) 1189–1214.

[19] W. Benz, E. Asphaug, Simulations of brittle solids using smooth particle hydrodynamics, Computer Physics Communication 87 (1995) 253–265.

[20] C. Zhang, X. Y. Hu, N. A. Adams, A generalized transport-velocity formulation for smoothed particle hydrodynamics, Journal of Computational Physics 337 (2017) 216–232.

[21] C. H. Lee, A. J. Gil, G. Greto, S. Kulasegaram, J. Bonet, A new jameson–schmidt–turkel smooth particle hydrodynamics algorithm for large strain explicit fast dynamics, Computer Methods in Applied Mechanics and Engineering 311 (2016) 71–111.

[22] C. H. Lee, A. J. Gil, A. Ghavamian, J. Bonet, A total lagrangian upwind smooth particle hydrodynamics algorithm for large strain explicit solid dynamics, Computer Methods in Applied Mechanics and Engineering 344 (2019) 209–250.

[23] M. Rezavand, C. Zhang, X. Hu, A weakly compressible SPH method for violent multi-phase flows with high density ratio, Journal of Computational Physics 402 (2020) 109092.

[24] Y.-X. Peng, A.-M. Zhang, F.-R. Ming, Particle regeneration technique for smoothed particle hydrodynamics in simulation of compressible multiphase flows, Computer Methods in Applied Mechanics and Engineering 376 (2021) 113653.

[25] B. Zheng, L. Sun, P. Yu, A novel interface method for two-dimensional multiphase SPH: Interface detection and surface tension formulation, Journal of Computational Physics 431 (2021) 110119.

[26] C. Antoci, M. Gallati, S. Sibilla, Numerical simulation of fluid–structure interaction by SPH, Computers & Structures 85 (2007) 879–890.

[27] X. Bian, Z. Li, G. E. Karniadakis, Multi-resolution flow simulations by smoothed particle hydrodynamics via domain decomposition, Journal of Computational Physics 297 (2015) 132–155.

[28] M. Toma, R. Chan-Akeley, J. Arias, G. D. Kurgansky, W. Mao, Fluid-structure interaction analyses of biological systems using smoothed particle hydrodynamics, Biology 10 (3) (2021) 185.

[29] C. Zhang, Y. Wei, F. Dias, X. Hu, An efficient fully lagrangian solver for modeling wave interaction with oscillating wave surge converter, Ocean Engineering 236 (2021) 109540.

[30] Z. Zhang, M. Khalid, T. Long, M. Liu, C. Shu, Improved element-particle coupling strategy with δ-sph and particle shifting for modeling sloshing

with rigid or deformable structures, Applied Ocean Research 114 (2021) 102774.

[31] R. Clayton, O. Bernus, E. Cherry, H. Dierckx, F. H. Fenton, L. Mirabella, A. V. Panfilov, F. B. Sachse, G. Seemann, H. Zhang, Models of cardiac tissue electrophysiology: Progress, challenges and open questions, Progress in Biophysics and Molecular Biology 104 (1-3) (2011) 22–48.

[32] S. Abboud, O. Berenfeld, D. Sadeh, Simulation of high-resolution QRS complex using a ventricular model with a fractal conduction system. Effects of ischemia on high-frequency QRS potentials., Circulation Research 68 (1991) 1751–1760.

[33] C. Vergara, S. Palamara, D. Catanzariti, F. Nobile, E. Faggiano, C. Pangrazzi, M. Centonze, M. Maines, A. Quarteroni, G. Vergara, Patient-specific generation of the purkinje network driven by clinical measurements of a normal propagation, Medical & Biological Engineering & Computing 52 (2014) 813–826.

[34] S. Tawara, Das Reizleitungssystem des Säugetierherzens: eine anatomisch-histologische Studie über das Atrioventrikularbündel und die Purkinjeschen Fäden, Fischer, 1906.

[35] R. J. Hall, Rapid interpretation of ekg's., Archives of Internal Medicine 128 (1971) 653–653.

[36] H. E. Çetingül, G. Plank, N. A. Trayanova, R. Vidal, Estimation of local orientations in fibrous structures with applications to the purkinje system, IEEE Transactions on Biomedical Engineering 58 (2011) 1762–1772.

[37] R. Bordas, K. Gillow, Q. Lou, I. Efimov, D. Gavaghan, P. Kohl, V. Grau, B. Rodriguez, Rabbit-specific ventricular model of cardiac electrophysiological function including specialized conduction system, Progress in Biophysics and Molecular biology 107 (2011) 90–100.

[38] D. S. Early, D. G. Long, Image reconstruction and enhanced resolution imaging from irregular samples, IEEE Transactions on Geoscience and Remote Sensing 39 (2001) 291–302.

[39] K. Ten Tusscher, A. V. Panfilov, Modelling of the ventricular conduction system, Progress in Biophysics and Molecular Biology 96 (2008) 152–170.

[40] O. Berenfeld, J. Jalife, Purkinje-muscle reentry as a mechanism of polymorphic ventricular arrhythmias in a 3-dimensional model of the ventricles, Circulation Research 82 (1998) 1063–1077.

[41] A. Lindenmayer, Mathematical models for cellular interactions in development i. filaments with one-sided inputs, Journal of Theoretical Biology 18 (1968) 280–299.

[42] T. Ijiri, T. Ashihara, T. Yamaguchi, K. Takayama, T. Igarashi, T. Shimada, T. Namba, R. Haraguchi, K. Nakazawa, A procedural method for modeling the purkinje fibers of the heart, The Journal of Physiological Sciences (2008) 0810170079–0810170079.

[43] F. S. Costabal, D. E. Hurtado, E. Kuhl, Generating purkinje networks in the human heart, Journal of Biomechanics 49 (2016) 2455–2465.

[44] R. Sebastian, V. Zimmerman, D. Romero, A. F. Frangi, Construction of a computational anatomical model of the peripheral cardiac conduction system, IEEE Transactions on Biomedical Engineering 58 (2011) 3479–3482.

[45] S. Palamara, C. Vergara, E. Faggiano, F. Nobile, An effective algorithm for the generation of patient-specific purkinje networks in computational electrocardiology, Journal of Computational Physics 283 (2015) 495–517.

[46] S. Palamara, C. Vergara, D. Catanzariti, E. Faggiano, C. Pangrazzi, M. Centonze, F. Nobile, M. Maines, A. Quarteroni, Computational generation of the purkinje network driven by clinical measurements: The case

of pathological propagations, International Journal for Numerical Methods in Biomedical Engineering 30 (2014) 1558–1577.

[47] R. M. Bordas, K. Gillow, D. Gavaghan, B. Rodríguez, D. Kay, A bidomain model of the ventricular specialized conduction system of the heart, SIAM Journal on Applied Mathematics 72 (2012) 1618–1643.

[48] E. J. Vigmond, C. Clements, Construction of a computer model to investigate sawtooth effects in the purkinje system, IEEE Transactions on Biomedical Engineering 54 (3) (2007) 389–399.

[49] D. Romero García, S. Aguilar, B. Bijnens, V. Zimmerman, P. M. Boyle, E. J. Vigmond, A. Frangi Caregnato, et al., Effects of the purkinje system and cardiac geometry on biventricular pacing: A model study, Annals Biomedical Engineering 38 (2010) 1388–98.

[50] C. Vergara, M. Lange, S. Palamara, T. Lassila, A. F. Frangi, A. Quarteroni, A coupled 3D-1D numerical monodomain solver for cardiac electrical activation in the myocardium with detailed purkinje network, Journal of Computational Physics 308 (2016) 218–238.

[51] T. P. Usyk, I. J. LeGrice, A. D. McCulloch, Computational model of three-dimensional cardiac electromechanics, Computing and Visualization in Science 4 (2002) 249–257.

[52] M. Landajuela, C. Vergara, A. Gerbi, L. Dedè, L. Formaggia, A. Quarteroni, Numerical approximation of the electromechanical coupling in the left ventricle with inclusion of the purkinje network, International Journal for Numerical Methods in Biomedical Engineering 34 (2018) e2984.

[53] W. Mao, K. Li, W. Sun, Fluid–structure interaction study of transcatheter aortic valve dynamics using smoothed particle hydrodynamics, Cardiovascular Engineering and Technology 7 (2016) 374–388.

[54] È. Lluch, M. De Craene, B. Bijnens, M. Sermesant, J. Noailly, O. Camara, H. G. Morales, Breaking the state of the heart: Meshless model for cardiac

mechanics, Biomechanics and Modeling in Mechanobiology 18 (2019) 1549–1561.

[55] L. Zhang, A. Ademiloye, K. Liew, Meshfree and particle methods in biomechanics: Prospects and challenges, Archives of Computational Methods in Engineering 26 (2019) 1547–1576.

[56] E. Lluch, O. Camara, R. Doste, B. Bijnens, M. De Craene, M. Sermesant, V. Y. Wang, M. P. Nash, H. G. Morales, Calibration of a fully coupled electromechanical meshless computational model of the heart with experimental data, Computer Methods in Applied Mechanics and Engineering 364 (2020) 112869.

[57] A. El-Baz, J. S. Suri, Level Set Method in Medical Imaging Segmentation, CRC Press, 2019.

[58] M. P. Nash, A. V. Panfilov, Electromechanical model of excitable tissue to study reentrant cardiac arrhythmias, Progress in Biophysics and Molecular Biology 85 (2004) 501–522.

[59] C. Zhang, M. Rezavand, Y. Zhu, Y. Yu, D. Wu, W. Zhang, J. Wang, X. Hu, SPHinXsys: An open-source multi-physics and multi-resolution library based on smoothed particle hydrodynamics, Computer Physics Communications (2021) 108066.

[60] C. Zhang, M. Rezavand, Y. Zhu, Y. Yu, D. Wu, W. Zhang, S. Zhang, J. Wang, X. Hu, SPHinXsys: An open-source meshless, multi-resolution and multi-physics library, Software Impacts 6 (2020) 100033.

[61] G. A. Holzapfel, R. W. Ogden, Constitutive modelling of passive myocardium: A structurally based framework for material characterization, Philosophical Transactions of the Royal Society A: Mathematical, Physical and Engineering Sciences 367 (2009) 3445–3475.

[62] J. Wong, S. Göktepe, E. Kuhl, Computational modeling of electrochemical coupling: A novel finite element approach towards ionic models for

cardiac electrophysiology, Computer Methods in Applied Mechanics and Engineering 200 (2011) 3139–3158.

[63] R. R. Aliev, A. V. Panfilov, A simple two-variable model of cardiac excitation, Chaos, Solitons & Fractals 7 (1996) 293–301.

[64] A. Panfilov, Three-dimensional organization of electrical turbulence in the heart, Physical Review E 59 (1999) R6251.

[65] Y. Zhu, C. Zhang, Y. Yu, X. Hu, A CAD-compatible body-fitted particle generator for arbitrarily complex geometry and its application to wave-structure interaction, Journal of Hydrodynamics 33 (2021) 195–206.

[66] M. A. Sherman, A. Seth, S. L. Delp, Simbody: Multibody dynamics for biomedical research, Procedia IUTAM 2 (2011) 241–261.

[67] H. Wendland, Piecewise polynomial, positive definite and compactly supported radial functions of minimal degree, Advances in Computational Mathematics 4 (1995) 389–396.

[68] J. P. Vila, Sph renormalized hybrid methods for conservation laws: applications to free surface flows, in: Meshfree methods for partial differential equations II, Springer, 2005, pp. 207–229.

[69] G. Strang, On the construction and comparison of difference schemes, SIAM Journal on Numerical Analysis 5 (1968) 506–517.

[70] J. P. Morris, P. J. Fox, Y. Zhu, Modeling low reynolds number incompressible flows using sph, Journal of computational physics 136 (1) (1997) 214–226.

[71] J. J. Monaghan, Smoothed particle hydrodynamics, Reports on progress in physics 68 (8) (2005) 1703.

[72] R. Fatehi, M. T. Manzari, Error estimation in smoothed particle hydrodynamics and a new scheme for second derivatives, Computers & Mathematics with Applications 61 (2) (2011) 482–498.

[73] C. Zhang, M. Rezavand, X. Hu, A multi-resolution SPH method for fluid-structure interactions, Journal of Computational Physics 429 (2021) 110028.

[74] A. S. Patelli, L. Dedè, T. Lassila, A. Bartezzaghi, A. Quarteroni, Isogeometric approximation of cardiac electrophysiology models on surfaces: An accuracy study with application to the human left atrium, Computer Methods in Applied Mechanics and Engineering 317 (2017) 248–273.

[75] A. Nitti, J. Kiendl, A. Gizzi, A. Reali, M. D. de Tullio, A curvilinear isogeometric framework for the electromechanical activation of thin muscular tissues, Computer Methods in Applied Mechanics and Engineering 382 (2021) 113877.

[76] P. C. Franzone, L. F. Pavarino, S. Scacchi, Mathematical cardiac electrophysiology, Vol. 13, Springer, 2014.

[77] P. Colli-Franzone, L. F. Pavarino, S. Scacchi, Mathematical and numerical methods for reaction-diffusion models in electrocardiology, in: Modeling of Physiological Flows, Springer, 2012, pp. 107–141.

[78] C. Mendez, W. J. Mueller, X. Urguiaga, Propagation of impulses across the purkinje fiber-muscle junctions in the dog heart, Circulation Research 26 (1970) 135–150.

[79] A. Quarteroni, T. Lassila, S. Rossi, R. Ruiz-Baier, Integrated heart—coupling multiscale and multiphysics models for the simulation of the cardiac function, Computer Methods in Applied Mechanics and Engineering 314 (2017) 345–407.

[80] J. P. Kucera, A. G. Kléber, S. Rohr, Slow conduction in cardiac tissue, ii: effects of branching tissue geometry, Circulation Research 83 (1998) 795–805.

[81] J. P. Kucera, Y. Rudy, Mechanistic insights into very slow conduction in branching cardiac tissue: A model study, Circulation Research 89 (2001) 799–806.